ULTRA-HIGH FREQUENCY ACOUSTIC IMPEDANCE IMAGING OF CANCER CELLS

By

Muhannad Fadhel

B.Sc. Ryerson University, 2011

Toronto, Ontario

A thesis

presented to Ryerson University

in partial fulfillment of the

requirements for the degree of

Master of Science

in the Program of

Biomedical Physics

Toronto, Ontario, Canada, 2014

© Muhannad Fadhel, 2014

AUTHOR'S DECLARATION

I hereby declare that I am the sole author of this thesis.

I authorize Ryerson University to lend this thesis to other institutions or individuals for the purpose of scholarly research.

I further authorize Ryerson University to reproduce this thesis by photocopying or by other means, in total or in part, at the request of other institutions or individuals for the purpose of scholarly research.

I understand that my thesis may be made electronically available to the public.

_____

Muhannad Fadhel

Ultra-High Frequency Acoustic Impedance Imaging of Cancer Cells

Master of Science, 2014

Muhannad Fadhel

Biomedical Physics, Ryerson University

ABSTRACT

Acoustic impedance maps of cells can be used to gain insight into its microstructures and physiological state. Information about the cell's microstructures can be acquired from the acoustic impedance map fluctuations. The maps can also help identify the dominant scattering source in cells. Furthermore, the cell's physiological state can be inferred from the average acoustic impedance values as many physiological changes in the cell are linked to the alteration in the mechanical properties. A method called acoustic impedance imaging has been used to measure the impedance of biological tissues. We used an acoustic microscope attached to a transducer with a center frequency of 375MHz to acquire acoustic impedance images of breast cancer cells. The generated images suggest that the nucleus has an acoustic impedance similar to the surrounding cytoplasm. Fluorescence and confocal microscopy were used to correlate acoustic impedance images with the cell microstructure (the nucleus). Simulation results demonstrate the system's capability in detecting cell microstructures close to the substrate. The average acoustic impedance were used to differentiate between single-live, clustered-live and clustered-fixed cancer cells with a measured values of 1.60±0.01 MRayl, 1.61±0.02 MRayl and 1.55±0.02 MRayl respectively.

ACKNOWLEDGMENTS

First, I would like to thank my supervisor Dr. Michael Kolios for all the motivation and guidance he gave me which will help me become a better physicist in the future. And for the time he spent from his busy days sharing his knowledge and experience. It has been a great journey and a great privilege to be his student.

Next, I would like to thank my committee meeting members Dr. Carl Kumaradas and Dr. Raffi Karshafian for helping me to understand many concepts and to improve my skills in articulating superior scientific arguments.

Also, I would like to thank my parents and siblings for helping me to realize my potential and for the huge motivation and support they provided.

Finally, I would like to thank all lab members for the great atmosphere they created and for orienting me on how to use new instruments and to better understand many concepts.

Table of Contents

LIST OF TABLES:

LIST OF FIGURES

LIST OF ABBREVIATIONS

MRI	magnetic resonance imaging
CT	X-ray computed tomography
BSC	backscatter coefficient
QUS	quantitative ultrasound
AIIM	acoustic impedance imaging method
BW	bandwidth
PBS	phosphate buffered saline

LIST OF SYMBOLS

σ_d	differential scattering cross-section (cm/sr)
θ, φ	spherical coordinates angles (degrees)
P	time averaged scattered power (watt)
Ω	solid angle (sr)
I	time average incident intensity (watt/cm^2)
k	wavenumber (μm^{-1})
a	scatterer size (μm)
Z	acoustic impedance (MRayl)
p	pressure (Pa)
v	particle velocity (m/s)
r	spatial position (m)
f	frequency (MHz)
ρ	density (kg/m^3)
c	speed of sound (m/s)
K	bulk modulus elasticity (Pa)
R	amplitude reflection coefficient
Z_n	acoustic impedance of the n material (MRayl)
θ_i, θ_t	incident, transmitted angle to the line normal to the surface (degrees)
κ_s, κ_0	compressibility of scatterer, background (1/Pa)
ρ_s, ρ_0	density of scatterer, background (kg/m^3)
$\bar{n}$	average number density of the scatterers (mm^{-3})
σ	poission's ratio
c_l , c_t	longitudinal, transverse speed of sound (m/s)
γ^2	fluctuation in the acoustic impedance
b_γ	correlation coefficient for the scattering medium
S_s, S_r	power spectrum of the sample, reference
η	backscatter coefficient (sr^{-1}cm^{-2})
α	attenuation coefficient (μm^{-1})
C	acoustic concentration (mm^{-3})
n	number density of the scatterers (mm^{-3})
Z_s, Z_0	acoustic impedance of the scattering source, background (MRayl)
η_s	measured BSC of the sample (sr^{-1}cm^{-2})
η_E	estimated BSC (sr^{-1}cm^{-2})

V_s	volume of a scatterer (μm^3)
F_a	gaussian form factor
a_{eff}	effective diameter (μm)
θ_a	½ the aperture angle (degrees)
T_{c-o}	transmitted signal from the coupling fluid to the slide
R_{o-s}	reflected signal at the slide-sample boundaries
R_{o-r}	reflected signal at the slide-reference boundaries
T_{o-c}	transmitted signal from the slide to the coupling fluid
R_{ax}, R_{lat}	axial, lateral resolution (μm)
A_o	amplitude of the incident signal
A_r, A_s	amplitude of the reflected signal from the reference, sample
Z_{r}, Z_{PE}	acoustic impedance of the reference, polystyrene (MRayl)
Z_{S_a}	apparent acoustic impedance of the sample (MRayl)
Z_{S_t}	true acoustic impedance of the sample (MRayl)
c_s, c_r	longitudinal speed of sound of the sample, reference (m/s)
T_{c-PE}	transmitted signal from the interface between the coupling fluid to the polystyrene layer
R_{PE-s}	reflected signal at the polystyrene and sample boundary
R_{PE-r}	reflected signal at the polystyrene and reference boundary
T_{PE-c}	transmitted signal from the polystyrene to the coupling fluid
p_i	incident pressure function (MPa)
A	amplitude of the negative peak pressure (MPa)
f_o	central frequency (MHz)

CHAPTER 1: INTRODUCTION

1.1 MOTIVATION

Ultrasound became a well-accepted imaging modality in the early 1970s when the first gray-scale ultrasound image with nonlinear compression dynamic range was presented [1]. The compression reduced the dynamic range of an image, which made it possible to visualize more information about tissue structures. Later, significant progress was made to understand ultrasound interaction with tissues in more detail, which allowed for the development of new ultrasound imaging techniques. Ultrasound has several advantages over its competing imaging modalities—magnetic resonance imaging (MRI) and X-ray computed tomography (CT). The three main advantages of ultrasound imaging are its ability to image tissues in real time, relative low cost and lack of harmful radiation [2]. Conventional ultrasound images are based on the analysis of the reflectivity of the tissue as a function of depth. Frequency analysis of the scattered signal is not currently used clinically. Careful analysis of the backscattered frequency spectrum has been utilized in laboratories to extract more information about tissue microstructures and physiological changes [3-7]. Three-dimensional acoustic impedance maps can be used to acquire the backscattered frequency spectrum. The main objective of this thesis is to use acoustic impedance imaging method to measure the acoustic impedance of cancer cells, and correlate them to microstructures in the cell.

1.2 DIAGNOSTIC ULTRASOUND

Ultrasound is a mechanical wave with a frequency higher than 20 kHz. It propagates through media by the compression and rarefaction of particles. Any variations in the density or compressibility of the medium can create distortion in the ultrasound waves. The scattered

ultrasound waves can be detected to attain information about tissues. For example in liver steatosis, a condition where the lipid level in liver cells increases, a change in effective density occurs due to fat deposits in liver cells. This can be detected ultrasonically, through an increase in the backscattered signal [8]. Cirrhosis can also be detected ultrasonically [9]. Cirrhosis is the loss of liver function due to the replacement of liver tissue by connective tissue. Connective tissue has different mechanical properties, which enable distinction between a normal and a diseased liver. In the kidney, ultrasound can detect inflammatory, vascular and infiltration problems [10]. Another use of ultrasound is the diagnosis of breast cancer through detecting changes of mechanical properties due to abnormal growth [11, 12]. Breast cancer is the most common malignant tumor in the world among women [12]. The sensitivity and specificity of sonography, a method used to detect breast cancer, in detecting malignancy are 50% and 91.8%, respectively [12]. In most cases, a biopsy is needed to confirm sonography and to differentiate between benign and malignant breast tumors [13, 14]. Biopsies are expensive, invasive, and time consuming. In addition, a limited volume of the suspected lesion is sampled, and therefore even if there is a tumor present, the biopsy might be negative.

Time domain and frequency domain analysis of the backscattered signals from a biological sample gives information about the microstructures of the sample and its physiological state [13, 15]. Cancer tissues might have different microstructures and physiological processes relative to normal tissues. A careful analysis of the time and frequency content in the backscattered signals has the potential to better utilize ultrasound for the diagnosis of cancer and possibly decrease the use of biopsy in detecting breast cancer. However, the origins of the frequency content of the backscattered signal, and how it changes

between malignant and normal cells, are not fully understood. This is due to the existence of many factors which contribute to the backscattered signal.

1.3 The Physics of Ultrasound Scattering

The interaction of ultrasound with a medium is characterized by attenuation. Attenuation is the loss of ultrasound wave intensity as it propagates through a medium. This occurs due to the conversion of mechanical energy into thermal energy (ultrasound absorption) and scattering of the wave (ultrasound scattering). Scattering is the redirection of ultrasound wave in a range of directions different than the incident wave due to localized non-uniformities in the medium [16].

As ultrasound waves propagate through a medium, changes in the mechanical properties of the medium causes the ultrasound waves to scatter. The scattered ultrasound signal is measured by the differential scattering cross-section (σ_d) [16]:

$$\sigma_d\,(\theta,\varphi) = \frac{P(\theta,\varphi)}{I\,\Omega} \tag{1.1}$$

where θ, φ are spherical coordinates angles, P is the time averaged scattered power, Ω is the solid angle and I is the time average incident intensity. The differential scattering cross-section has a unit of cm^2/sr (area/solid angle), which represents the likelihood of ultrasound waves to scatter at specific angle. The differential scattering cross-section is a function of the ultrasound wavelength and changes in the medium mechanical properties. The scattered ultrasound signal is related to the ratio of the scatterer size to incident ultrasound wavelength; these two parameters are typically combined into one parameter called *ka*—the product of wavenumber

$\left(k = \frac{2\pi}{\lambda}\right)$ and scatterer size (a). Changes in the mechanical properties can be accounted for through a parameter called acoustic impedance. Acoustic impedance (Z) is defined as the amount of pressure generated due to the vibration of the molecules as shown below:

$$Z\,(r,f) = \frac{p(r,f)}{v(r,f)} \tag{1.2}$$

where p is the pressure, v is the particle velocity, r is the spatial position and f is the frequency. The unit used for acoustic impedance is Rayleigh (Rayl) which is equal to kg/s.m^2. Equation 1.2 refers to the specific acoustic impedance which depends on both frequency and spatial position. This dependence is due to the phase difference between the pressure and particle velocity created in viscous medium through friction loss. Assuming a plane incident wave in an inviscous fluid medium equation 1.2 simplifies into:

$$Z\ = \rho c = \sqrt{K\rho} \tag{1.3}$$

where ρ, c and K are the density, speed of sound and bulk modulus elasticity of the medium. Equation 1.3 is referred to as the characteristic acoustic impedance which is constant for a specific homogeneous medium and does not depend on the frequency and spatial position [16]. In this thesis the acoustic impedance refers to the characteristic acoustic impedance.

In order to calculate the theoretical differential scattering cross-section for a given sample (Equation 1.1), the Helmholtz wave equation is solved for the appropriate scattering geometry and boundary conditions [17]. Two extreme cases have been derived which are ka>>1 and ka<<1. The first case occurs when the scatterer source size is significantly larger than the wavelength (ka>>1) [16]. In this case, both the shape and size of the scatterer do not

contribute to the scattered signal, instead only changes in the mechanical properties can be used to predict the scattered signals. This typically makes it possible to treat the scattering surface as a planar surface. In this case the strength of the scattered signal can be represented by [16]:

$$R = \frac{Z_2\cos(\theta_i) - Z_1\cos(\theta_t)}{Z_2\cos(\theta_i) + Z_1\cos(\theta_t)} \tag{1.4}$$

where R is the scattered pressure amplitude over the incident pressure amplitude, $Z_1$and Z_2 respectively are the acoustic impedance of the first and second materials, θ_i and θ_t respectively are the incident angle and the transmitted angle to the line normal to the surface as shown in figure 1.1.

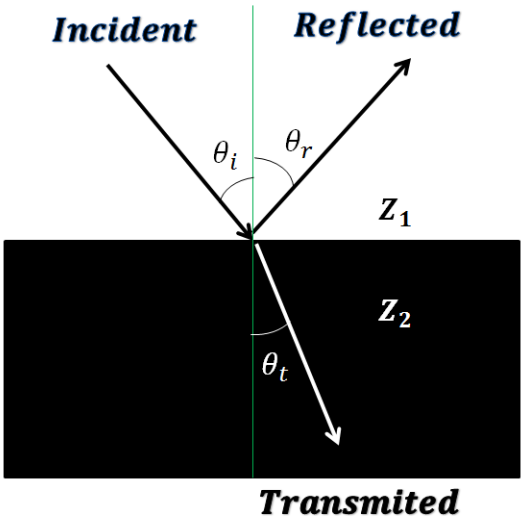

Figure 1.1 Schematic of incident ultrasound wave approaching an interface of two different materials.

The second case, called Rayleigh scattering, happens when the scatterer size is significantly smaller than the wavelength (ka<<1). In this case, the shape of the scatterer source does not contribute to the scattered signal. The Rayleigh scattering equation is [16]:

$$\sigma_d(\theta) = \bar{n}\frac{k^4V^2}{16\pi^2}\left[\frac{\kappa_s - \kappa_0}{\kappa_0} + \frac{3(\rho_s - \rho_0)}{2\rho_s + \rho_0}\cos(\theta)\right]^2 \quad (1.5)$$

where κ_s, ρ_s and κ_0, ρ_0 are the compressibility $(1/K)$ and density of scatterer and background, respectively. $\bar{n}$ is the average number density of the scatterer. A portion of the scattered signal is due to changes in the compressibility between the scatterer and the background, and is not angle dependent (Equation 1.5). This is referred to as the monopole term, which in the case of a spherical scatterer causes the scatterer source to oscillate equally in all directions. In contrast, the scattered signal due to changes in the density between the scatterer and the background are angle dependent (Equation 1.5). This is referred to as the dipole term, which causes the scatterer source to oscillate parallel to the propagating wave [16].

The rest of the cases are in between the two extremes mentioned above, when the scatterer size is comparable to the wavenumber. In these cases, ultrasound scattering becomes more complex. The differential scattering cross-section for radiating pressure scattered from a single uniform spherical or cylindrical scatterer source has been derived by Faran in 1951. The solutions are functions of scatterer size, wavenumber, Poission's ratio, and density and compressibility of the scatterer source and the surrounding background [18]. The Poission's ratio (σ) is related to the speed of sound of transverse and longitudinal waves:

$$\sigma = \frac{1}{2}\frac{c_l^2 - 2c_t^2}{c_l^2 - c_t^2} \quad (1.6)$$

where c_l and c_t are the longitudinal and transverse speeds of sound in a specific medium. Liquid and gas media do not support transverse waves due to the weak interaction between their particles. Biological soft tissues are mainly composed of water which does not support

transvers waves (c_t approaches 0); this causes the Poission's ratio to approach 0.5 (Equation 1.6). Biological soft tissues are complex due to the presence of scatterers with different shapes and mechanical properties. The Faran equation assumes single scattering source with a known shape (spherical or cylindrical). The wave equation for heterogeneous scattering medium is a better representation of wave propagation for biological soft tissues, but it requires knowledge of the mechanical properties of the tissues.

1.4 THE SCATTERED PRESSURE FROM HETEROGENEOUS MEDIUM

In biological tissues, both the density and compressibility fluctuates spatially throughout the tissue. The wave equation for a heterogeneous medium accounts for these fluctuations. Several assumptions have been made to simplify the solution of the wave equation for a heterogeneous medium. First, the transducer focal depth is significantly larger than the transmitted wavelength. Second, the incident pressure wave at the focal point, where the scattering cross section is calculated, is planar. Third, the medium is a weak scattering source—in other words, there are small fluctuations in the density and the compressibility of tissues (also known as the Born approximation) [10]. Assuming weak scattering, the scattered wave has an amplitude much smaller in magnitude compared to the incident wave and therefore multiple scattering is ignored. Finally, it is assumed that the scattering sources are randomly distributed. Organized scatterers can lead to constructive or destructive interferences, which can increase or decreased the backscattered signal at a specific frequency. These assumptions simplify solving the wave equation for the differential scattering cross-section (σ_d) of a heterogeneous medium to:

$$\sigma_d = \frac{k^4\langle\gamma^2\rangle}{16\pi^2}\int_{-\infty}^{\infty} b_\gamma(\Delta r)\, e^{-i\boldsymbol{K}.\boldsymbol{\Delta r}}\, d\boldsymbol{\Delta r} \tag{1.7}$$

where $\boldsymbol{K}$ is the change in wavenumber ($|\boldsymbol{K}| = 2k$ in case of backscattered signal ($\sigma_d\ (\pi, 0)$)), $\langle\gamma^2\rangle$ is the mean-square fluctuation in the acoustic impedance, $b_\gamma(\Delta r)$ is the correlation coefficient for the scattering medium, and $\mathbf{\Delta r}$ is the change between two positions in the medium. Equation 1.7 was derived to help in understanding the interaction of ultrasound waves with biological tissues (since biological tissues are a heterogeneous medium with fluctuations in the acoustic impedance). However, the difficulty in measuring $\langle\gamma^2\rangle$ and $b_\gamma(\Delta r)$ (the two parameters can be combined through the spatial fluctuation of the acoustic impedance map) of tissues made it challenging to solve for the backscattered signal.

An approach, called the reference phantom technique, has been used to analyze the frequency content of the backscattered signals experimentally to acquire information about the interaction of ultrasound wave with biological tissues.

1.5 THE REFERENCE PHANTOM TECHNIQUE

The reference phantom technique is a method developed by Lin Xin Yao et. al. in 1990 to calculate the backscatter coefficient (BSC), which is the differential scattering cross-section for $\sigma_d\ (\pi, 0)$ (Equation 1.1) per unit volume [19]. Using this technique, different instruments generating the same ultrasound frequencies should give the same BSC if they are used to image the same sample. The reference phantom technique makes it possible to analyze the frequency content of backscattered signals in real time at clinical settings [20]. This method was confirmed experimentally by comparing the calculated BSC from different ultrasound instruments [21]. In this method, the following equation has been used to calculate the BSC:

$$\frac{S_s(k,d)}{S_r(k,d)} = \frac{\eta_s(k)}{\eta_r(k)} \frac{e^{-4\alpha_s\,(k)d}}{e^{-4\alpha_r(k)d}} \tag{1.8}$$

where S is the power spectrum of the backscattered signal, η is the BSC, and α is the attenuation coefficient. $d = ct/2$ where c is the speed of sound and t is the time the signal is being mapped for. The subscripts s and r denote for the sample and reference respectively. The reference phantom method uses a reference phantom with a known power spectrum, attenuation and BSC to calculate the BSC of a sample using the same experimental setup. The BSC has been used in analyzing the frequency contents for a scattered signal, independent of the instrumentation used to acquire the signal. This is important since quantitative ultrasound (QUS) techniques take into account the frequency dependence of the BSC to infer tissue structure.

1.6 Quantitative Ultrasound

Many QUS parameters have been used to characterize tissues. Two QUS parameters that have been used frequently to characterize tissue, calculated from the BSC are: the effective scatterer size and the acoustic concentration [13]. The effective scatterer size is related to the volume of the scatterer source. The acoustic concentration is related to the concentration of the scatterers and the impedance mismatch between the scatterer and the background as shown in the equation below:

$$C = n\left(\frac{Z_s - Z_0}{Z_0}\right)^2 \tag{1.9}$$

where C is the acoustic concentration, n is the number density of the scatterer, Z_s is the impedance of the scattering source and Z_0 is the impedance of the background. These two

parameters are calculated by computing the smallest mean-square error (argmin) to fit the measured BSC to an estimated BSC, as shown in the equation below:

$$a = \text{argmin}\left[\int_{k_{\min}}^{k_{\max}} [log(\eta_s(k)) - log(G\eta_E(k,a))]^2 dk\right] \quad (1.10)$$

where η_s is the measured BSC of the sample, η_E is the estimated BSC, $k_{\max}$ and $k_{\min}$ are the maximum and minimum wavenumber used for fitting and it depend on the estimated BSC, a is the scatterer size, and G is used to calculate the acoustic concentration as shown in the equation below:

$$C = \frac{G}{(V_s(a))^2} \quad (1.11)$$

V_s is the volume of the scatterer source. The estimated BSC is calculated theoretically either by using a well known model (e.g. Faran) or by multiplying the Rayleigh scattering equation with a correction factor. The correction factor is called a form factor which is calculated by taking the square of the three dimensional Fourier transform of the assumed scatterer shape [13]. The form factor approach has been used due to its simplicity—it requires less parameters and it can be used to account for any scatterer shape. One of the form factors that is widely used to characterize biological tissues is the Gaussian form factor. This form factor assumes that the impedance mismatch between the scatterer and background occurs gradually [22]. The Gaussian form factor is shown below:

$$F_a(2k) = e^{-0.827k^2a_{\text{eff}}^2} \quad (1.12)$$

a_{eff} is the effective diameter which is related to the correlation distance (d), the minimum spatial separation between two scatterers to receive two independent signals, through $a_{\text{eff}} = 3.11d$. The use of these theoretical models in calculating QUS parameters has helped in differentiating between different biological tissues clinical ultrasound images were unable to detect.

1.7 ADVANTAGES OF QUS

QUS parameters can be used to characterize tissues. This is achievable since the parameters derived represent changes in scatterer source number, size, shape, compressibility, and density of the medium [18]. It has been hypothesized that QUS parameters can be used to detect changes in biological structures that cannot be detected by a conventional ultrasound, with greater sensitivity to smaller changes [23].

Previous studies showed the advantages of using QUS parameters in characterizing tissues microstructures such as ocular, myocardial, liver, and kidney tissues [19, 24-27]. Ocular cancer can be recognized as an increase in effective scatterer size [28]. Myocardial infarction can be detected as an increase in the BSC [29]. Solid tumor in liver is related to a decrease in the BSC [19, 30]. Tissue characterization of the kidney demonstrates the possibility in differentiating normal kidney vs. renal cell carcinoma vs. oncocytoma, based on the BSC [10, 31]. QUS has also been used to monitor high intensity focused ultrasound (HIFU) treatments [6], detect cancerous lymph nodes [23], and identify various forms of cell death [32, 33].

Clinical ultrasound machines use frequency ranges between 1-15MHz, which gives a penetration depth of 5-15cm [16]. Frequency analysis of ultrasound backscattered signal can be

used to find a correlation between tissue structures and scatterer source e.g. the nephron and the glomerulus [10]. As the frequency of ultrasound increases, the resolution also increases which enables resolving smaller scatterers. At frequency around 25MHz, it is hypothesized that the QUS techniques can resolve-scatterers at the cellular level [4]. Using this frequency scientists were able to differentiate between different cancer tissues [3, 5]. Results demonstrate a clear difference in both the effective scatterer size and acoustic concentration between rats' mammary fibroadenomas and mouse carcinomas [3, 5]. In contrast, ultrasound quantification to differentiate between mouse carcinoma vs. sarcoma was not achieved using both effective scatterer size and acoustic concentration parameters [4]. Nonetheless, the optical images of the two cancers revealed a clear difference. To improve the capability of QUS parameters to differentiate between diseased tissues, better denotation of the measured effective scatterer source and acoustic concentration are required. This can be achieved by improving our understanding of the shape and properties of scatterers at the cellular level.

1.8 IDENTIFYING THE DOMINANT SCATTERER SOURCE USING HIGH FREQUENCY ULTRASOUND

Tissue scatterer source identification can help in describing tissues' morphology, therefore improving ultrasound diagnostic capabilities and treatment monitoring. Many research studies have been done to determine the scatterer source in tissues. It is hypothesized that the nucleus is the main scatterer in biological structures [33-35]. One experiment which supports this was done by comparing the integrated BSC of human epithelial kidney cells with the multinucleated human epithelial kidney cell [34]. The results revealed no difference in the BSC between the normal and the multinucleated epithelial kidney cells. Since the cell size is

different but the nucleus size being the same between normal and multinucleated cells, the similar in BSC was hypothesized to be due to similar scatterer source (the nucleus).

Another study done by Oelze and Zachary hypothesizes that the whole cell acts as the major scattering source [4]. This was done by comparing the size of carcinoma cells to the measured effective scatterer size of carcinoma tissue and carcinoma cell pellet. The results revealed no statistical difference between all three sizes. The hypothesized conclusion was the cell is the main scattering source. A clear understanding of the scatterer source in biological tissues is still unclear, due to the lack of knowledge about spatial maps of acoustic impedance of biological tissues.

In a study done by Mamou el. al. [13, 36] they presented a method which can be used to determine the scatterer source in tissues from the 3D acoustic impedance map (3DZM). In this method, the solution of the wave equation from a heterogeneous medium (Equation 1.7) is used to calculate the BSC using 3DZM. The calculated BSC is compared to the measured BSC from the same heterogeneous medium (tissue) [13, 36]. The 3DZM is obtained by taking a tissue and slice it into thin sections. The sliced sections are stained using haematoxylin and eosin staining (H&E) imaged using optical microscopy. A transformation, rotation, and stretching is applied to each slice to align the images into a 3D histological volume. The 3DZM is created by assigning an impedance values to the optical 3D histological volume. The impedance map values are obtained from look-up tables of acoustic impedance values. This method was unable to identify the scatterer source. In the study, it was stated that more accurate impedance values were required to be used for wider range of scatterers and that the variation within a single scatterer had to be accounted for [13, 36].

1.9 Importance of Measuring the Acoustic Impedance of Biological Structures

One of the advantages of measuring the acoustic impedance of biological structures is to help in identifying the scattering source. In addition, acoustic impedance values have been used to obtain information about the cell physiology and its environment [15, 37, 38]. Acoustic impedance values are sensitive to changes in density, speed of sound or elastic properties (Equation 1.3). Many physiological changes in the cell, such as cell division, cell motility, cell adhesion, gene expression, signal transduction and apoptosis, have been linked to alteration in the elastic properties of the membrane and the intracellular fluid [38-41]. For example, detected changes in the elastic properties of red blood cells have been correlated to the maturation of specific parasites [42]. In addition, changes in the elastic properties of the arterial have been associated with diabetes, hypertension, stroke, heart failure, and renal failure [43-46]. Beside elasticity, speeds of sound have been used to differentiate between blood as its going through coagulation and retraction [47], evaluate enzymes activities and differentiating between gastritis, ulcer and cancer in the stomach [7]. The importance of measuring the acoustic impedance arises due to its direct correlation to biological structures, dynamics and thermodynamics of biological molecules [7].

Many techniques have been developed to measure the mechanical properties of biological structures. The elasticity of biological structures is related to the resistivity of its structures to deform. To measure elasticity, an external force is applied to deform the biological structures. The ratio of the applied force to the deformation is used to measure elasticity. The external force is created mechanically, or through applying electric or magnetic fields. The applied force can deform portion of the cell, the whole cell or population of cells [40]. Some of

these techniques are: atomic force microscopy [48], magnetic tweezers [49], optical tweezers [50], micropipette aspiration [51], shear-flow methods [52], and stretching devices [53].

All the techniques mentioned above require applying stress on the biological structures in order to measure its mechanical properties. Measuring the mechanical properties of biological structures using acoustic microscopy has been desired due to the minimal stress it applies on the sample, the relative high resolution and speed [54]. Measuring the mechanical properties of biological structures using acoustic microscopy can be done by analyzing the time-domain or the frequency-domain of the backscattered signal [38, 54]. Using the time-domain signal, a method called pulse-echo can be used to measure both the density and speed of sound. Speed of sound is measured by comparing the time shift from the sample and the reference with a known speed of sound [38, 55]. Density is measured from the calculated speed of sound and using the amplitude of the reflected signal (Equation 1.3). Using the frequency-domain signal, measuring the density and speed of sound can be obtained by using phase analysis or interpolation of the voltage vs. frequency plot [43, 54, 56]. Both methods use the voltage vs. frequency plot to measure the mechanical properties of the sample. In addition, acoustic impedance can be measured directly using acoustic microscopy [55, 57].

1.10 Acoustic Impedance Imaging Method

Recently, a method to measure the acoustic impedance in tissues using acoustic microscopy has been developed by Hozumi et. al. (2005). This method, namely acoustic impedance imaging method (AIIM), assumes the scatterer source is significantly larger than the ultrasound wavelength and the incident ultrasound beam is normal to the sample. The reflection coefficient due to an impedance mismatch is shown in equation 1.4. AIIM uses a

reference material with known acoustic impedance to calculate the acoustic impedance of an unknown sample [57]. The setup of AIIM goes in the following order: transducer, coupling fluid, slide, and the mounted sample, which is different from acoustic microscopy imaging for which the sample is place on top of the slide (figure 1.2). The transducer is focused on the slide-sample boundary. There are two properties of the slide that must be taken into consideration to successfully image the sample using AIIM. First, the slide must have a low impedance mismatch relative to the coupling fluid (<4MRayl) so that the transmitted signal through the slide-coupling fluid boundary will be maximized [57]. Second, the slide has to be thin in order to reduce the attenuation of the signal through the slide itself.

The acoustic images acquired using acoustic microscopy have a different setup compared to the setup used in the AIIM. The setup of acoustic microscopy imaging goes in the following order: transducer, coupling fluid, the sample and slide. There are two advantages of AIIM over the acoustic microscopy imaging. First, it improves the lateral resolution by focusing the ultrasound wave to a smaller focal spot as it propagates through the slide. Second, the sample, by virtue of being mounted on the slide, will always have a controlled planar boundary. Consequently, the incident ultrasound is always perpendicular to the slide-sample interface which allows the calculation of acoustic impedance. This point is important in case of imaging cells, since the morphology of cells cannot be controlled. Although the wave propagation through the slide increases the lateral resolution, the signal also gets attenuated as it propagates through the slide. This results in a lower signal-noise ratio (SNR). Moreover, a calibration needs to be applied in order to account for the shear wave created in the solid slide

and the finite angle of the transducer as it enters the coupling fluid-slide-sample boundaries [58].

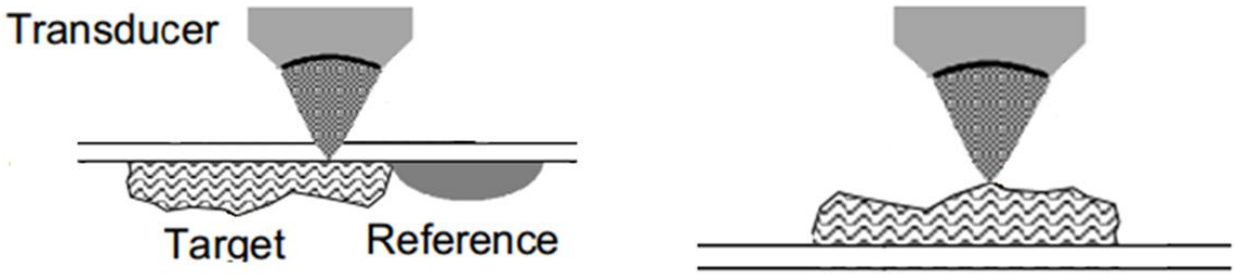

Figure 1.2 On the left is a schematic for the geometric setup used in the acoustic impedance imaging method. On the right is a schematic for the geometric setup used in the acoustic microscopy imaging method.

1.11 CALIBRATION FOR AIIM

The measured acoustic impedance of the sample using equation 1.4 is different than the actual acoustic impedance of the sample. The relationship between the measured and actual acoustic impedance is shown below [59]:

$$Z_{s_a} = \frac{1 + \frac{A_s(Z_{s_t}, c_s, \theta_a)}{A_r(Z_{r_t}, c_r, \theta_a)} \frac{Z_r - Z_{o_l}}{Z_r + Z_{o_l}}}{1 - \frac{A_s(Z_{s_t}, c_s, \theta_a)}{A_r(Z_{r_t}, c_r, \theta_a)} \frac{Z_r - Z_{o_l}}{Z_r + Z_{o_l}}} Z_{o_l} \tag{1.13}$$

where Z_{s_a} is the measured acoustic impedance of the sample using equation 1.4, Z_{s_t} is the actual acoustic impedance of the sample, θ_a is ½ the aperture angle, the subscripts l, s, r and o denote for the longitudinal wave, sample, reference and slide. A_s/A_r is the ratio of the amplitude backscattered from the sample over the amplitude backscattered from the reference as shown below:

$$\frac{A_s(Z_{s_a}, c_s, \theta_a)}{A_r(Z_{r_a}, c_r, \theta_a)} = \frac{\int_0^{\theta_a} T_{c-o} R_{o-s} T_{o-c} d\theta}{\int_0^{\theta_a} T_{c-o} R_{o-r} T_{o-c} d\theta} \tag{1.14}$$

where T_{c-o} is the transmitted signal from the coupling fluid to the slide, R_{o-s} and R_{o-r} are the reflected signal at the slide-sample and slide-reference boundaries, respectively, T_{o-c} is the transmitted signal from the slide to the coupling fluid as shown in figure 1.3. All these parameters are solid-fluid or fluid-solid interfaces which can be calculated from the equations below [60]:

$$T_{c-o} = \frac{2\sqrt{BC_1}}{1 + C_1(1 - 2A)} \tag{1.15}$$

$$A = \sin(\theta_{o_t}) \sin(2\theta_{o_t}) \left[\cos(\theta_{o_t}) - \left(\frac{c_{o_t}}{c_{o_l}}\right) \cos(\theta_{o_l})\right]$$

$$B = \left(cos(2\theta_{o_t})\right)^2, \qquad C_1 = \frac{Z_{o_l} \cos(\theta_a)}{Z_c \cos(\theta_{o_l})}$$

$$R_{o-s} = \frac{E - F - C_s}{E + F + C_s}, \qquad R_{o-r} = \frac{E - F - C_r}{E + F + C_r} \tag{1.16}$$

$$C_s = \frac{Z_s \cos(\theta_{o_l})}{Z_{o_l} \cos(\theta_s)}, \qquad C_r = \frac{Z_r \cos(\theta_{o_l})}{Z_{o_l} \cos(\theta_r)}$$

$$E = \left(cos(2\theta_{o_t})\right)^2, \qquad F = \left(\frac{c_{o_t}}{c_{o_l}}\right)^2 \sin(2\theta_{o_l}) \sin(2\theta_{o_t})$$

$$T_{o-c} = \frac{\sqrt{4EC_2}}{E + F + C_2} \tag{1.17}$$

$$C_2 = \frac{Z_c \cos(\theta_{o_l})}{Z_{o_l} \cos(\theta_a)}$$

the subscript t is for transverse wave. The angles are calculated using Snell's law:

$$\theta_{o_l} = arcsin\left(\frac{c_{o_l}}{c_c} sin(\theta_a)\right),$$

$$\theta_{o_t} = arcsin\left(\frac{c_{o_t}}{c_{o_l}} sin(\theta_{o_l})\right),$$

$$\theta_s = arcsin\left(\frac{c_s}{c_{o_l}} sin(\theta_{o_l})\right), and$$

$$\theta_r = arcsin\left(\frac{c_r}{c_{o_l}} sin(\theta_{o_l})\right).$$

The results of AIIM are 2D image representing the acoustic impedance map of the sample at the slide interface. This map can be correlated to the sample morphology by using optical microscopy, histological staining or fluorescence microscopy.

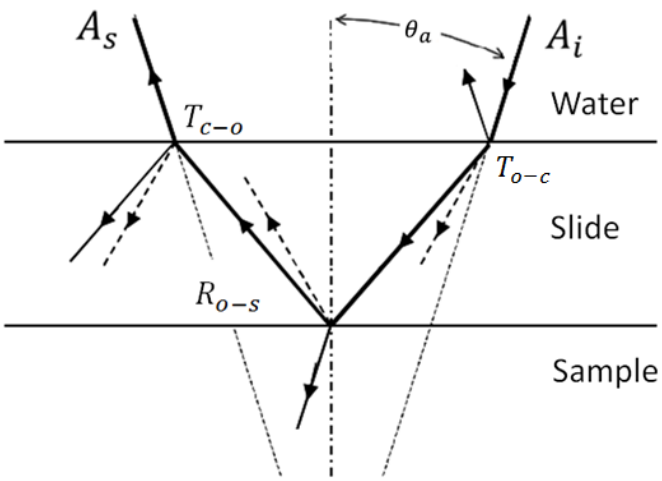

Figure 1.3 Acoustic wave path as the wave propagates from the transducer to the sample and back to the transducer.

1.12 Fluorescence Microscopy

Fluorescence microscopy is similar to conventional optic microscopy [61]. Fluorescence microscopy uses high intensity lasers with a narrow bandwidth that excite a desired molecule within a sample. Optical microscopy uses much lower intensity with wider bandwidth (all visible wavelengths). The main purpose of fluorescence microscopy is to increase the signal from the

sample while decreasing background noise [61]. The principle of fluorescence microscopy is applied by illuminating the specimen with a specific wavelength of light. The light is absorbed by the specimen and reemitted at a longer wavelength. This change in wavelength allows the detection of specific characteristics within the specimen. The molecules that absorb and emit light are called fluorophores.

Fluorophores are unique molecules that contain conjugated double bonds [61]. Naturally, they are rare to be found in biological structures and in this case the biological structure will be considered autofluorescent. All other cases require introducing external fluorophores which bind directly or indirectly to biological structures. Well-known examples of fluorophores which bind directly to biological structures are Hoechst and CellTracker Orange. Hoechst is a molecule which binds to the minor groove of the DNA [62]. This molecule is used to stain the nucleus. CellTracker Orange is composed of CMTMR (5-(and-6)-(((4-chloromethyl) benzoyl) amino) tetramethylrhodamine which reacts to the thiols group in the presence of a protein called esterase (present inside cells) which binds the CellTracker Orange molecule to the thiols group. The thiols group mainly exists in glutathione S-transferase which is a protein common in the cytoplasm. Therefore, CellTracker Orange is used to stain the cytoplasm. Fluorophores which bind indirectly to biological structures require introducing an external protein molecule. This protein has two binding sites: one site binds directly to the desired target molecule inside the cell or extracellular matrix, and the second site binds to the fluorophore molecule.

If the specimen contains molecules such as fluorophores, the absorbed light is reemitted with lower energy. The absorbed energy is directly related to the frequency of the illuminated light. As fluorophores absorb light their electrons jump from a ground electronic state to an excited state. The absorbed light can cause an electron to jump from one orbital to an orbital further away from the nucleus. The excited state has more energy which causes alterations in the vibrational and rotational state of the fluorophores. The excited state of the fluorophores reemits light almost instantaneously with different wavelengths—the reemitted light has lower energy. The emitted light is separated from the illuminated light based on the difference in wavelength. The challenging part in fluorescence microscopy is finding the proper fluorophores to bind to the desired target. An advanced type of fluorescence microscopy is called confocal microscopy which allows higher resolution and contrast.

Thick sample with fluorophores above and below the focal point can be problematic when imaged using fluorescence microscopy. This is due to the light radiated from the fluorophores in focus and out of focus that will be detected by the lens. The illumination of the out of focus fluorophores causes the images to be blurred [63, 64]. Unlike fluorescence microscopy, confocal microscopy uses a pinhole to block the light illuminated by out of focus fluorophores to obtain sharper images [63, 64]. The pinhole reduces the thickness of the optical sectioning to 0.5-1.5µm vs. >50 µm for a conventional fluorescence microscopy [64]. Thinner optical sections grant the reconstruction of 3D images by changing the depth of focus. In addition, confocal is used to obtain images with higher contrast and resolution than a conventional fluorescence microscopy.

1.13 Hypothesis and Specific Aims

The main objective of this study is to use ultra-high frequency AIIM to calculate the acoustic impedance map of cancer cells. This can be used as an input for the 3DZM maps to identify the main scatterer source and help in understanding the mechanical properties of an individual cancer cell and its physiological state. The hypothesis of this study is that AIIM can be used to measure the acoustic impedance of microstructures in cancer cells. The specific aims are to a) develop the AIIM methodology to measure the acoustic impedance b) validate the AIIM method with materials of known acoustic impedance and c) to combine the AIIM measurements with fluorescence measurements to identify the target microstructures. To accomplish the above, a solid layer had to be identified that was thin (<100μm) so the reflected signal will not be attenuated and that had a low acoustic impedance (<4MRayl) to increase the transmitted signal through the coupling fluid and the solid layer boundary. Moreover, the material should allow the cell to attach firmly to it.

CHAPTER 2: MATERIALS AND METHODS

2.1 CELL PREPARATION

The cell line used in this experiment was MCF-7. MCF-7 is an invasive breast duct carcinoma cell line (ATCC, Manassas, VA). Cells were grown in Dulbecco's modified Eagle's medium (DMEM) supplemented with 10% fetal bovine serum (FBS) in a humidified incubator maintained at 37°C and 5% CO_2. Cells were maintained in the exponential growth phase, and passaged using trypsin dissociation when the flasks were 80-90% confluent.

24 hours prior to the experiment, the old media was aspirated leaving the cells which have been attached to the T25 flask. The cells were washed and aspirated with 1ml of phosphate buffered saline (PBS). 1ml of trypsin was added to the cells. The cells were incubated. After three minutes, the flask was examined under a microscope to verify that the cells were in suspension. If the cells were not suspended, the flask was gently shaken physically. 4ml of media was added to the flask then transferred into a 15ml tube. The tube was centrifuged at 150g for 3min at room temperature. The media was removed and 6ml of new media was added to the cells and mixed. 1ml of cells containing media (approximately 300 000 cells) was added to 9ml of growth media. The 10ml mixture was transported into a culture system made of two parallel polystyrene thin membranes (NUNC Opticell, Thermo Fisher Scientific, Waltham, MA) and left in the incubator.

2 hours prior to the experiment, 10µl of 10mM of Celltracker Orange (Life Technologies, Carlsbad, CA) and 10ml of media replaced the old media in the Opticell. The Opticell was incubated for 30 minutes. After, the media was removed and the Opticell was washed with

10ml of PBS. 10ml of media and 200µl of Hoechst 33342 (Life Technologies, Carlsbad, CA) were added to the Opticell and incubated for 30 minutes.

2.2 IMAGING

2.2.1 ACOUSTIC AND FLUORESCENCE IMAGES

A custom built scanning acoustic microscope (SASAM, Kibero GmbH, Saarbrucken, Germany), based on an IX81 microscope body (Olympus, Central Valley, PA), capable of both acoustic and fluorescent imaging was used in these experiments. Acoustic imaging was completed using transducer with a center frequency of 375MHz, a bandwidth of 150MHz, and an aperture angle of 60°. The axial resolution (R_{ax}) and lateral resolution (R_{lat}) are calculated using the equations below [65]:

$$R_{\mathrm{ax}} = \frac{1}{2}\frac{c}{\mathrm{BW}} \qquad R_{\mathrm{lat}} = \frac{\bar{\lambda}}{2\tan(\theta_a)} \tag{2.1}$$

where $\bar{\lambda}$ is the average wavelength, c is the speed of sound and BW is the bandwidth of the transducer. The axial and lateral resolutions of the transducer in water were calculated to be 5.1µm and 3.6µm respectively. Fluorescent microscopy images were taken with a monochrome CCD camera with a resolution of 1392 x 1040 pixels (Lumenera, Ottawa, Ontario, Canada). The entire microscope, including the sample, is kept in a climate controlled chamber at 36.0±0.2^{o}C. The setup is shown in figure 2.1. The coupling fluid used was water. Media was used as the background in order to image cells and its acoustic impedance was measured using AIIM. Equation 2.2 was used to calculate the amplitude of the incident signal (A_o):

$$A_r = \frac{A_o\left(Z_{PE_l} - Z_r\right)}{\left(Z_{PE_l} + Z_r\right)} \tag{2.2}$$

where A_r is the amplitude of the reflected signal due to the impedance mismatch between the polystyrene substrate and the reference, *Z* is the acoustic impedance. The subscripts *PE*, *r* and *l* are polystyrene, reference, and longitudinal. The equation below was used to solve for the apparent acoustic impedance of the sample (Z_{S_a}) without accounting for the shear waves and the finite angle of the transducer:

$$A_s = \frac{A_o\left(Z_{PE_l} - Z_{s_a}\right)}{\left(Z_{PE_l} + Z_{s_a}\right)} \tag{2.3}$$

where A_s is the amplitude of the reflected signal due to the impedance mismatch between the polystyrene layer and the sample.

To image cells, the samples prepared were imaged both optically and acoustically. The ultrasound backscatter radiofrequency signals were obtained by scanning the transducer in the x-y plane with step size of 1µm and a field of view ranging from 40µm-100µm depending on the cell size. The apparent acoustic impedance images were obtained by calculating Z_{S_a} of each radiofrequency signal. Green and ultraviolet light were used to image the Hoechst and Celltracker Orange stains respectively. 20 single cells and 10 clustered cells were imaged using both acoustic and fluorescence microscopy.

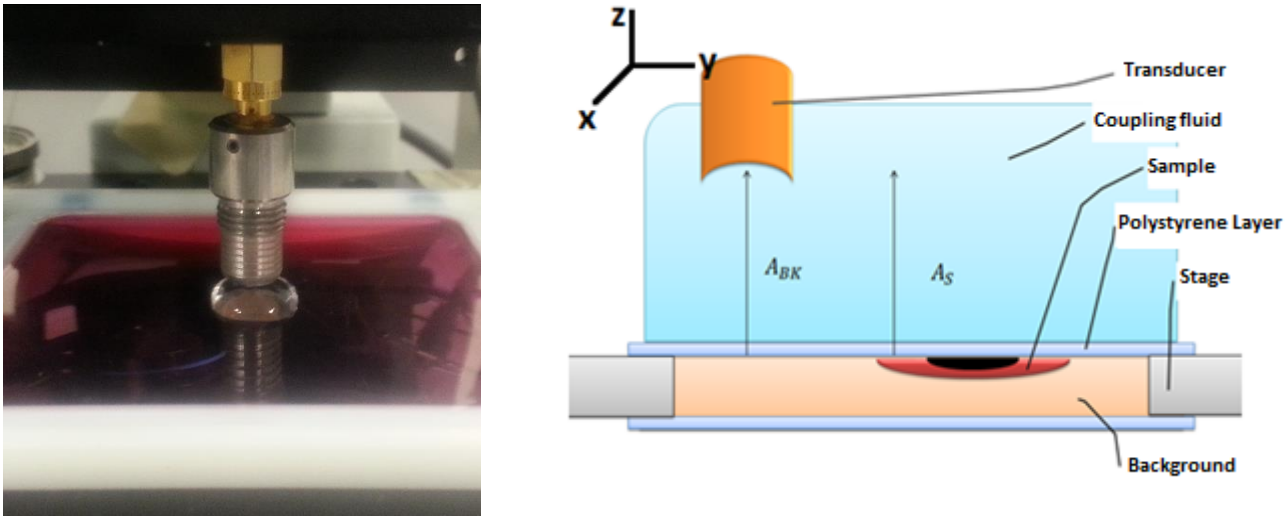

Figure 2.1 The setup of AIIM experiment. On the left is a view of the trasnducer positoned above the coupling fluid, stage with the sample and the optical microscopy. On the right is a schematic of the acoustic microscopy setup. Transducer used had center frequency of 375MHz, the coupling fluid used was water, sample used was MCF-7 cell, the culture system used was Opticells and background used was media (DMEM and 10% FBS).

2.2.2 Fixing cells

After imaging the cells using the acoustic microscopy, the media in the Opticell was replaced with 10ml of 10% formalin and left at room temperature for 15 minutes. After 10ml of PBS was added to the Opticell to replace the formalin. An additional 7 acoustic impedance and fluorescence images of clustered cells were acquired. The clustered-fixed cells were compared to the clustered-live and single-live cells.

2.2.3 Acoustic Impedance calibration

A calibration is applied to find the acoustic impedance of the sample (Z_{S_t}) after accounting for both the shear waves created in the polystyrene and the finite angle of the transducer. This was done by substituting A_o from equation 2.2 in equation 2.3 and rearrange it to solve for Z_{S_a}:

$$Z_{s_a} = \frac{1 + \frac{A_s}{A_r}\frac{Z_r - Z_{PE_l}}{Z_r + Z_{PE_l}}}{1 - \frac{A_s}{A_r}\frac{Z_r - Z_{PE_l}}{Z_r + Z_{PE_l}}} Z_{PE_l} \tag{2.4}$$

A_s/A_r in the equation above assumes fluid-fluid boundaries (no shear waves) with normal incident angle. To eliminate these assumptions, A_s/A_r is calculated using the equation below:

$$\frac{A_s(Z_{s_t}, c_s, \theta_a)}{A_r(Z_{r_t}, c_r, \theta_a)} = \frac{\int_0^{\theta_a} T_{c-PE}(\theta) R_{PE-s}(Z_{s_t}, c_s, \theta) T_{PE-c}(Z_{s_t}, c_s, \theta) d\theta}{\int_0^{\theta_a} T_{c-PE}(\theta) R_{PE-r}(Z_{r_t}, c_r, \theta) T_{PE-c}(Z_{r_t}, c_r, \theta) d\theta} \tag{2.5}$$

where θ_a is ½ the aperture angle of the ultrasound transducer, c_s and c_r are the longitudinal speed of sound of the sample and reference, T_{c-PE} is the transmitted signal from the interface between the coupling fluid to the polystyrene layer, R_{PE-s} or R_{PE-r} is the reflected signal at the polystyrene and sample or reference boundary, T_{PE-c} is the transmitted signal from the polystyrene to the coupling fluid. All these interfaces are solid-fluid or fluid-solid have been derived by Mayer (1965) [60]. The integral in equation 2.5 is computed through the summation of angle (θ) intervals of 0.01°. Now equation 2.4 can be rewritten as:

$$Z_{S_a} = \frac{1 + \frac{A_s(Z_{s_t}, c_s, \theta_a)}{A_r(Z_{r_t}, c_r, \theta_a)}\frac{Z_r - Z_{PE_l}}{Z_r + Z_{PE_l}}}{1 - \frac{A_s(Z_{s_t}, c_s, \theta_a)}{A_r(Z_{r_t}, c_r, \theta_a)}\frac{Z_r - Z_{PE_l}}{Z_r + Z_{PE_l}}} Z_{PE_l} \tag{2.6}$$

the equation above was used to determine the correlation between the apparent and true acoustic impedance.

To test this calibration, the acoustic impedance of water was measured using air as a reference. This was done by applying AIIM to image 50µm x 50µm in dimensions with 2µm step

size at 10 different positions. The same method was used to measure the acoustic impedance of the media and the PBS, since they were the backgrounds in case of imaging live and fixed cells, respectively. The speed of sound of the backgrounds was needed to apply the calibration. The speed of sound of media and PBS were calculated by dividing the acoustic impedance over the density. The densities of the backgrounds were measured by taking the ratio of the mass over the volume—using electronic balance (Scientech, Boulder, CO) and 5ml pipette (Fisher Scientific Company, Ottawa, Ontario).

2.2.4 IMAGE ANALYSIS

2.2.4.1 SIZE COMPARISON

Acoustic impedance and fluorescent images of the cytoplasm and nucleus (stained with Celltracker Orange and Hoechst, respectively) were superimposed for each single cell. A trace line was selected at a location within the image for which the difference between the cell size compared to the nucleus size (assessed through the fluorescent staining) was the largest. The trace lines were normalized so the minimum and maximum values, of the intensity in case of fluorescence microscopy and acoustic impedance values in cause of acoustic microscopy, were equal to 0 and 1. A size was obtained for each trace line by subtracting the first and last location when the normalized amplitude was 0.5 as show in figure 2.2. The size ratio of the trace line of fluorescence images labeled by Celltracker Orange stain over acoustic impedance images, and the trace line of fluorescence images labeled by Hoechst stain over acoustic impedance images were acquired. These calculations were done for all 20 single-live cells.

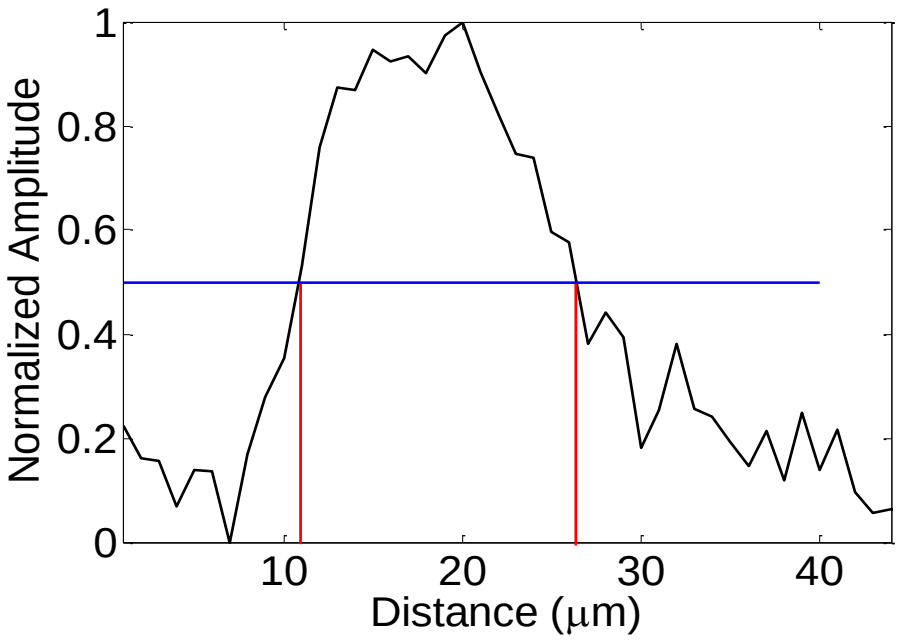

Figure 2.2 The method used to calculate size from a normalized trace line. The blue line is used to calculate the full width-half maximum, drawn at the normalized amplitude of 0.5. The distance between the intersections of the blue line and the black line (trace line) is acquired (red lines). The difference between the two x-axis readings is used to calculate the size.

2.2.4.2 ACQUIRING AVERAGE ACOUSTIC IMPEDANCE OF CELLS

The cells were segmented from the background using threshold and erosion. Thresholds were applied to all acoustic impedance images, to eliminate the background impedance. The thresholds were 1.575MRayl and 1.520MRayl in case of media and PBS as backgrounds, respectively. The threshold values were acquired from the average value of the first minima from the smoothed histogram of the acoustic impedance images. Smoothing was performed using a moving average filter of size 0.005MRayl. Next, the acoustic impedance images were eroded with two different disk shaped matrix of size 3µm and 7µm in diameter which are approximately one and two times the lateral resolution of the transducer in polystyrene. Erosion is a morphological image processing technique which removes pixels from the object

boundaries (cell boundaries in this experiment). The number of the removed pixels at the boundaries depends on the size of the erosion with a larger erosion size removing more pixels at the boundaries. The purpose of erosion is to reduce the effect of the point spread function of the transducer on the measured acoustic impedance values. The non-eliminated pixels were averaged for each image and the standard deviation was calculated. The mean of the average acoustic impedance and standard deviation were calculated for the three different groups (single-live, clustered-live and clustered-fixed cells). The means were compared using a multiple comparison test to examine which comparisons are statistically different.

2.3 CONFOCAL IMAGES

A Zeiss LSM 700 confocal laser scanning microscope (Oberkochen, Germeny) with 40x oil lens was used to obtain 3D images of MCF-7 cells. Hoechst and CellTracker Orange stains were used to image the nucleus and cytoplasm respectively. The axial step size was 0.33µm. The depth of the nucleus from the polystyrene layer was measured by subtracting the depth of the image were the CellTracker Orange stain first appear with the depth of the image were the Hoechst stain appeared (indicating the cell nucleus) with a diameter of at least 4µm (the approximate wavelength of the ultrasound waves in water). 16 cells were imaged confocally to obtain a perspective about the depth of the nucleus from the substrate.

2.4 SIMULATIONS

To better understand the effect of the distance of microstructures from the substrate to the measured acoustic impedance, simulations were performed (COMSOL MultiPhysics, Stockholm, Sweden). The software uses the Helmholtz wave equation to solve for the scattered pressure. Three different material domains were used in the finite element software to

simulate the polystyrene substrate, the cytoplasm and the nucleus of the MCF-7 cells. Four simulations were run. The speed of sound and density of the materials used in these simulations are presented in table 2.1. Table 2.1 parameters represent postulated ranges of acoustic impedances of the nucleus (1.6-1.8MRayl) and cytoplasm (1.5-1.7MRayl) [13, 38, 54, 56]. The thickness of the middle layer varied between 0.1-4.0 µm and had a maximum element size of 0.05µm. The first and third layer had a thickness of 20.0µm and a maximum element size of 0.2µm. The width of all the layers was 5.0µm. The equation of incident pressure used was:

$$p_i(z,t) = -A\sin\left(2\pi f_o\left(t-\frac{z}{v}\right)\right)\exp\left(-4\left(\mathrm{BW}\left(t-\frac{z}{v}\right)\right)^2\right) \tag{2.7}$$

where p_i is the incident pressure function, a is the amplitude of the negative peak pressure (1MPa), f_o is the central frequency (375MHz), v is the speed of sound in water (1520m/s), BW is the bandwidth of the transducer (150MHz). t and z are the modeled time and spatial intervals, respectively. The time interval modeled was 0-1.5x10^{-6}s and the spatial interval modeled was the added thickness of all three layers. The time interval was determined so the incident pressure wave interferes with both first and second boundaries. The maximum amplitude of the reflected signal was measured. Using equation 2.8, the reflected pressure was replaced by acoustic impedance (Z_2):

$$\frac{p_r}{p_i} = \frac{Z_2 - Z_{PE}}{Z_2 + Z_{PE}} \tag{2.8}$$

where p_{ip} and p_{rp} are the amplitude of the incident and reflected signal, Z_{PE} is the acoustic impedance of the polystyrene layer. The calculated Z_2 vs. thickness of the middle layer, representing the cytoplasm thickness in-between the substrate and the nucleus, was plotted.

	Layer 1			Layer 2			Layer 3		
	Density (kg/m^3)	Speed of Sound (m/s)	Impedance (MRayl)	Density (kg/m^3)	Speed of Sound (m/s)	Impedance (MRayl)	Density (kg/m^3)	Speed of Sound (m/s)	Impedance (MRayl)
Simulation 1	1050	2340	2.46	1000	1500	1.50	1200	1500	1.80
Simulation 2	1050	2340	2.46	1000	1500	1.50	1000	1800	1.80
Simulation 3	1050	2340	2.46	1000	1700	1.70	1000	1600	1.60
Simulation 4	1050	2340	2.46	1133	1500	1.70	1067	1500	1.60

Table 2.1 Parameters used to simulate three consecutive layers with different densities and speed of sound. Layer 1, 2 and 3 are used to represent the properties of polystyrene, cytoplasm and nucleus.

CHAPTER 3: RESULTS

The acoustic impedance values of different cells were obtained using AIIM. The fluorescence confocal images were used to assess the morphology of a cell and to calculate the distance between the nucleus and the polystyrene substrate. The simulations were run to determine the effect of the distance between the nucleus and the polystyrene substrate on the measured 2D acoustic impedance images.

3.1 ACOUSTIC IMPEDANCE IMAGING

A representative radiofrequency signal collected from the middle of a cell and from a location within the media (background) are presented in figure 3.1. There are three distinct time intervals in the reflected radiofrequency signal. First, the time signal recorded in the interval between 1.390µs-1.405µs is due to the acoustic impedance mismatch between the polystyrene and the sample (cells) or background. Second, the signal recorded in the time interval between 1.405µs-1.415µs is due to the acoustic impedance mismatch with in the sample or background. Third, the signal recorded in the time interval between 1.420µs-1.440µs is potentially due to the leaky Rayleigh waves created at the coupling fluid and the polystyrene boundary [66]. After the acoustic impedance images were acquired from the radiofrequency signals and a calibration was needed to account for effects such as the shear waves created in the polystyrene. Acoustic impedance calibration plots are shown in figure 3.2 in case of air, media and PBS used as the reference. The densities used in the calibration were measured to be 0.99±0.01g/cm^3 and 1.04±0.01g/cm^3 for media and PBS at 36^{o}C. AIIM accuracy was tested by measuring the acoustic impedance of water. The measured acoustic impedance of water was

1.5129±0.0009 MRayl. The next step was to measure the average acoustic impedance of the backgrounds used in the experiments: media and PBS. The results are presented in table 3.1.

2D acoustic impedance maps of cells were acquired using AIIM after applying the correction presented in figure 3.2. The results of three acoustic impedance images are presented in figure 3.3 adjacent to fluorescence microscopy images of the same cells with stained nucleus (blue) and cytoplasm (red), and line traces of the normalized acoustic impedance images (black), fluorescence images labeled by Hoechst (blue) and fluorescence images labeled by CellTracker Orange (red). The acoustic impedance and fluorescence images of live and fixed cells are shown in figure 3.4.

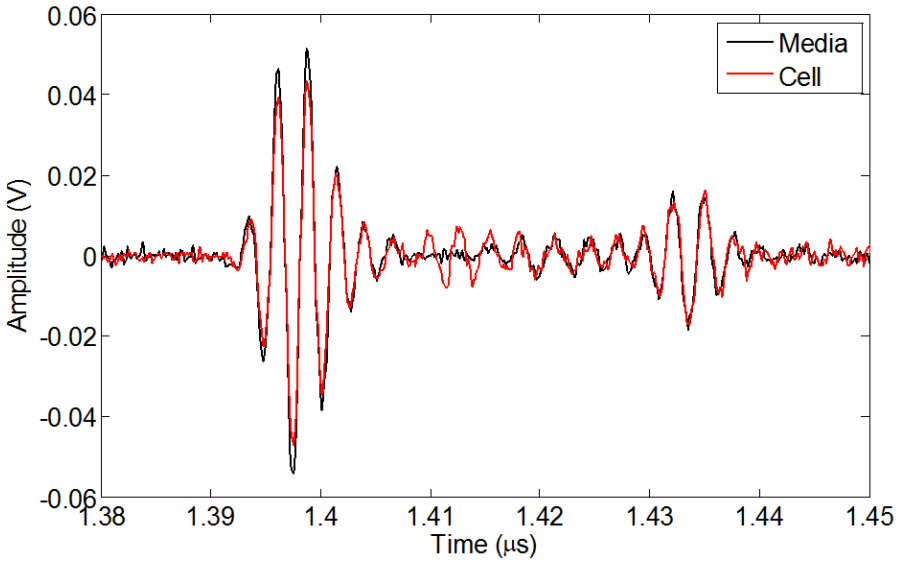

Figure 3.1 Plot comparing the radiofrequency signal reflected from the middle of a cell (red) and the radiofrequency signal reflected from the media (black). 1.390μs-1.405μs time interval is due to the acoustic impedance mismatch between the polystyrene and the sample. 1.405μs-1.415μs time interval is due to the acoustic impedance mismatch with in the sample. 1.420μs-1.440μs time interval is potentially due to the leaky Rayleigh waves created at the coupling fluid and the polystyrene boundary.

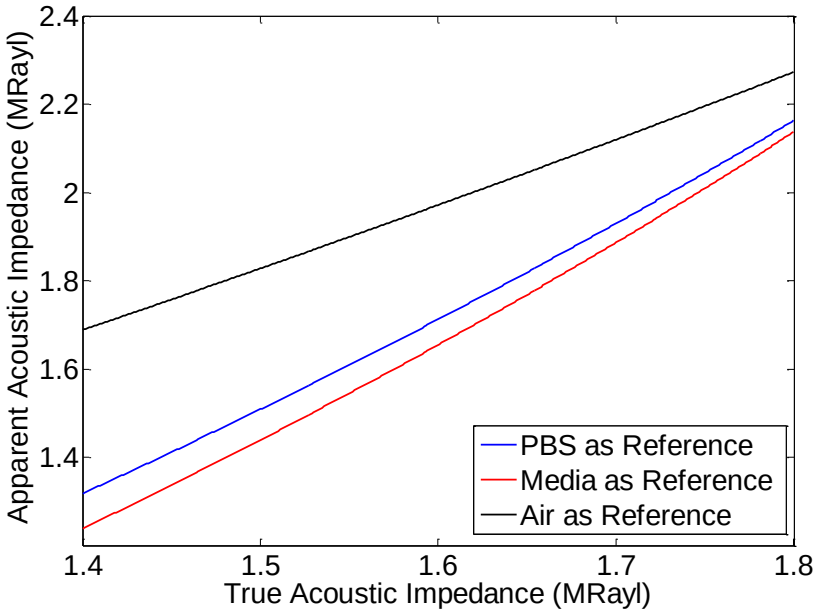

Figure 3.2 AIIM calibration plot. Parameters used are: $Z_{PE_l} = 2.46MRayl, c_{PE_t} = 1150m/s, c_{PE_l} = 2340m/s, c_{air} = 352m/s, Z_{air} = 0.0004MRayl.$

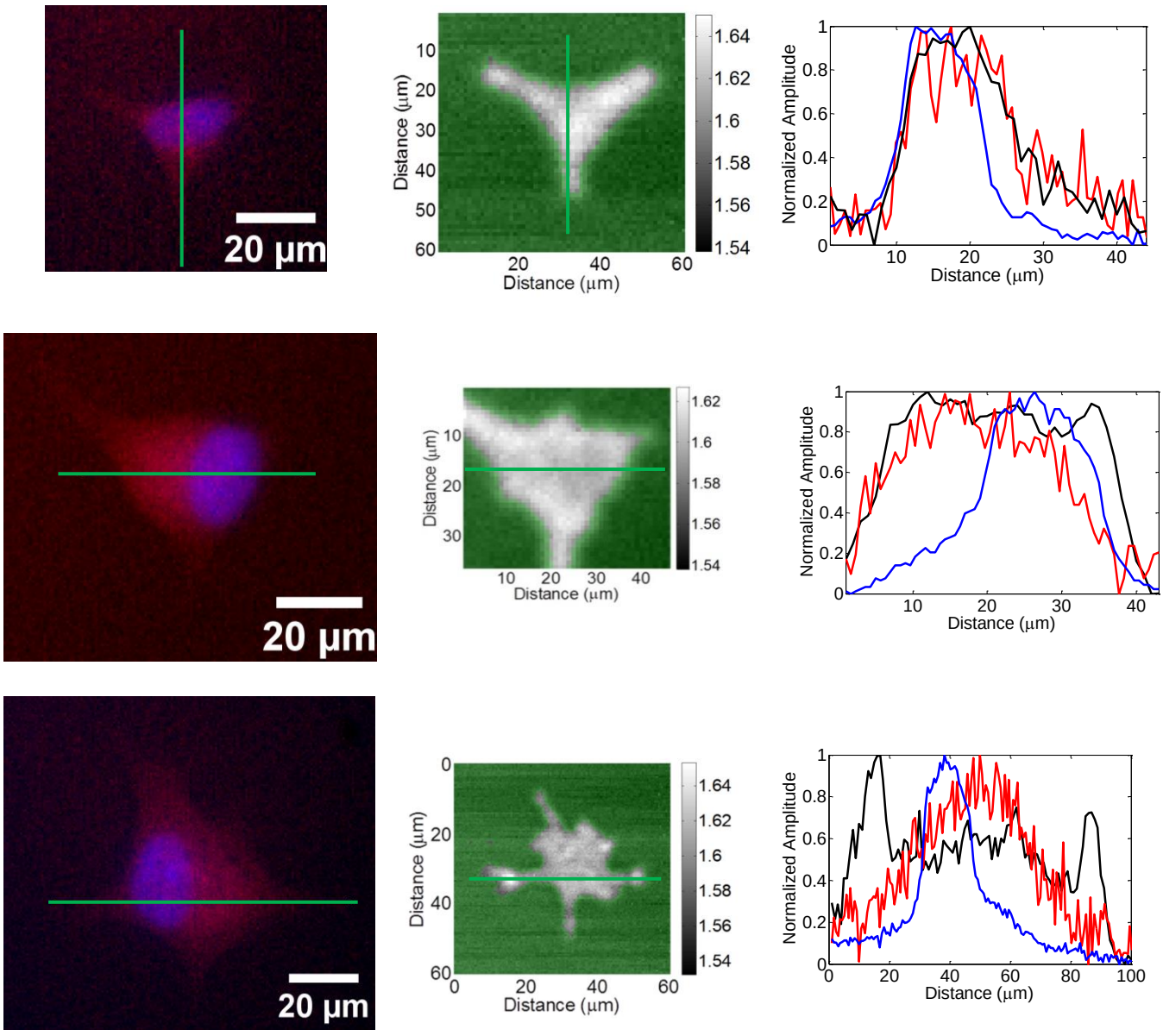

Figure 3.3 Comparing acoustic impedance images with fluorescence images of MCF-7 cells. The images on the left are fluorescent images of three single cells imaged using Hoechst and CellTracker Orange stains pseudo-colored with blue and red respectively. The middle images are the same cells imaged using AIIM. The green transparent overlays represent the eliminated pixels to calculate the average acoustic impedance using 3µm erosion disk. The graphs on the right denote trace of the green lines of the normalized acoustic impedance (black line), normalized intensity of the Hoechst and CellTracker Orange stains (blue and red respectively) at the locations denoted in the images in the left and center of the figure.

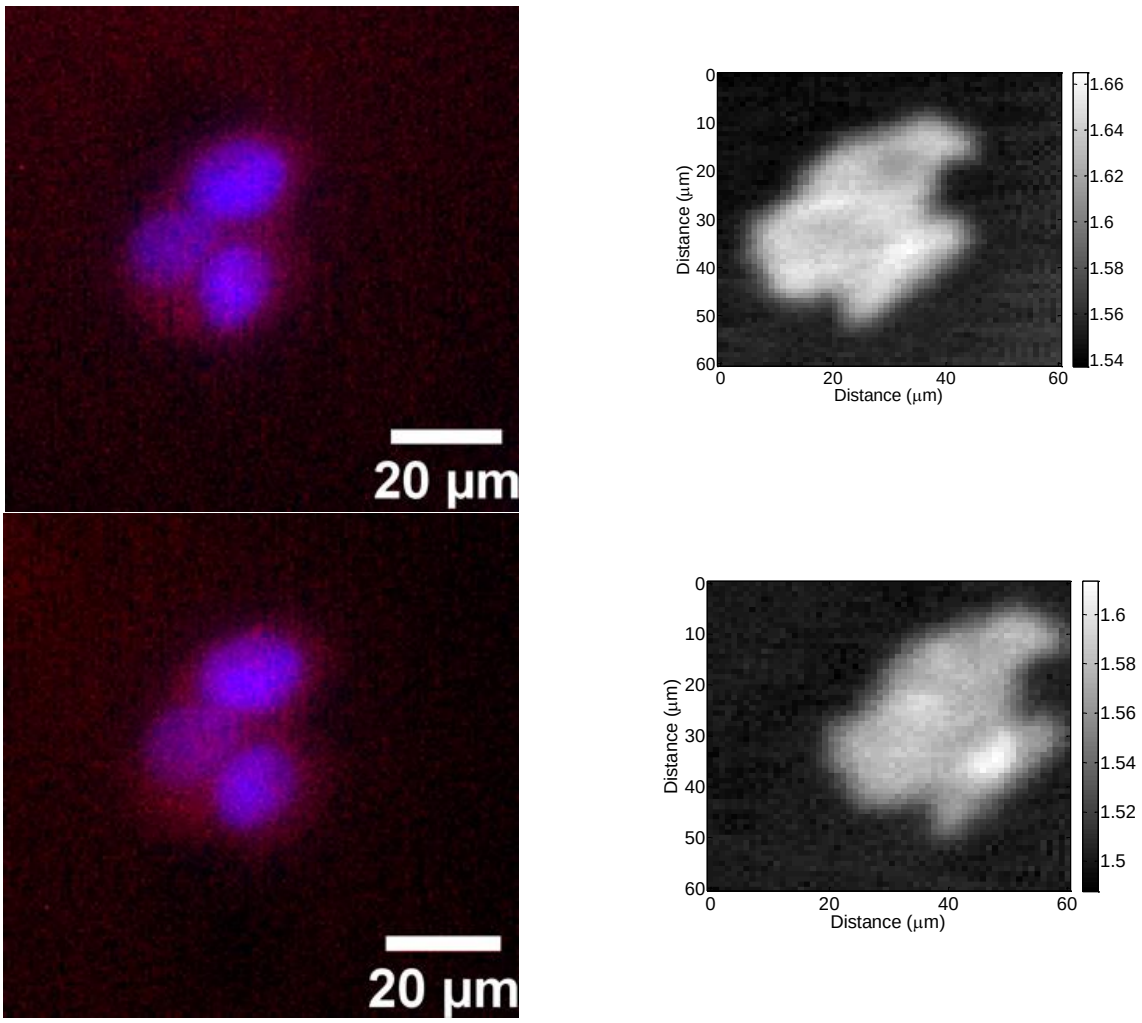

Figure 3.4 Comparing live and fixed cells. The left images are fluorescence images of cells stained with Hoechst and CellTracker Orange pseudo-colored with blue and red respectively. The right images are cells imaged using AIIM. The top are images of live cells, bottom are images of the same cells fixed.

	Average Acoustic Impedance (MRayl)	Average Standard Deviation (MRayl)
Water	1.5129±0.0084	0.0009±0.0004
Media	1.5527±0.0076	0.0007±0.0003
PBS	1.5012±0.0050	0.0006±0.0004

Table 3.1 Results of the average acoustic impedance and standard deviation for water, media and PBS using air as a reference. The average acoustic impedance column is calculated by taking the mean acoustic impedance of each acoustic impedance images at 10 different positions and averaging the results.

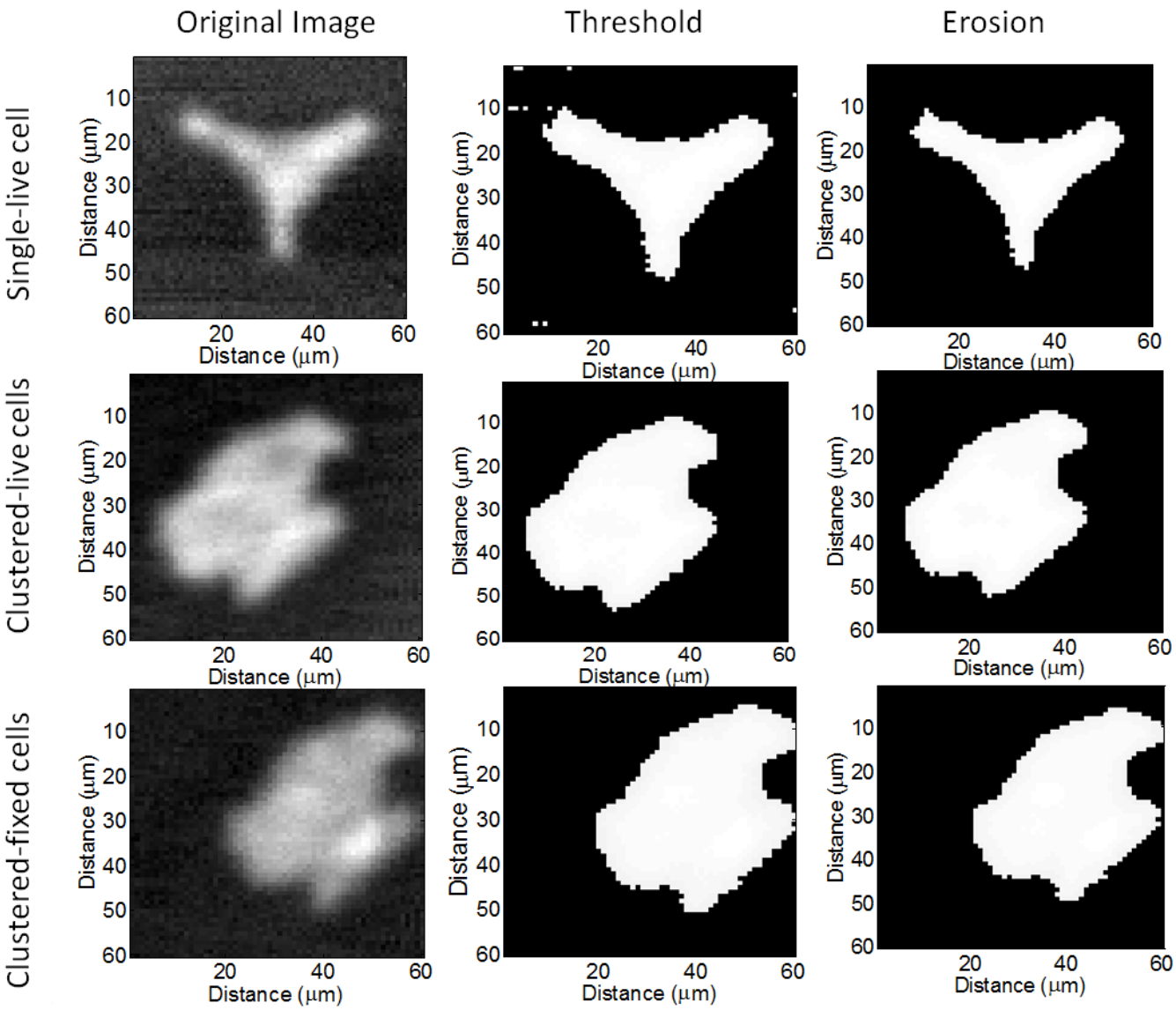

Figure 3.5 Images used to demonstrate the image analysis processes used to segment the cell/s. Left to right respectively are the acoustic impedance images, the acoustic impedance images after applying threshold of 1.575MRayl for the top two images (background used was media) and 1.520MRayl for the bottom image (background used was PBS), and acoustic impedance images after applying the threshold and 3μm erosion disk. Top to bottom respectively are single-live cell, clustered-live cells and clustered-fixed cells.

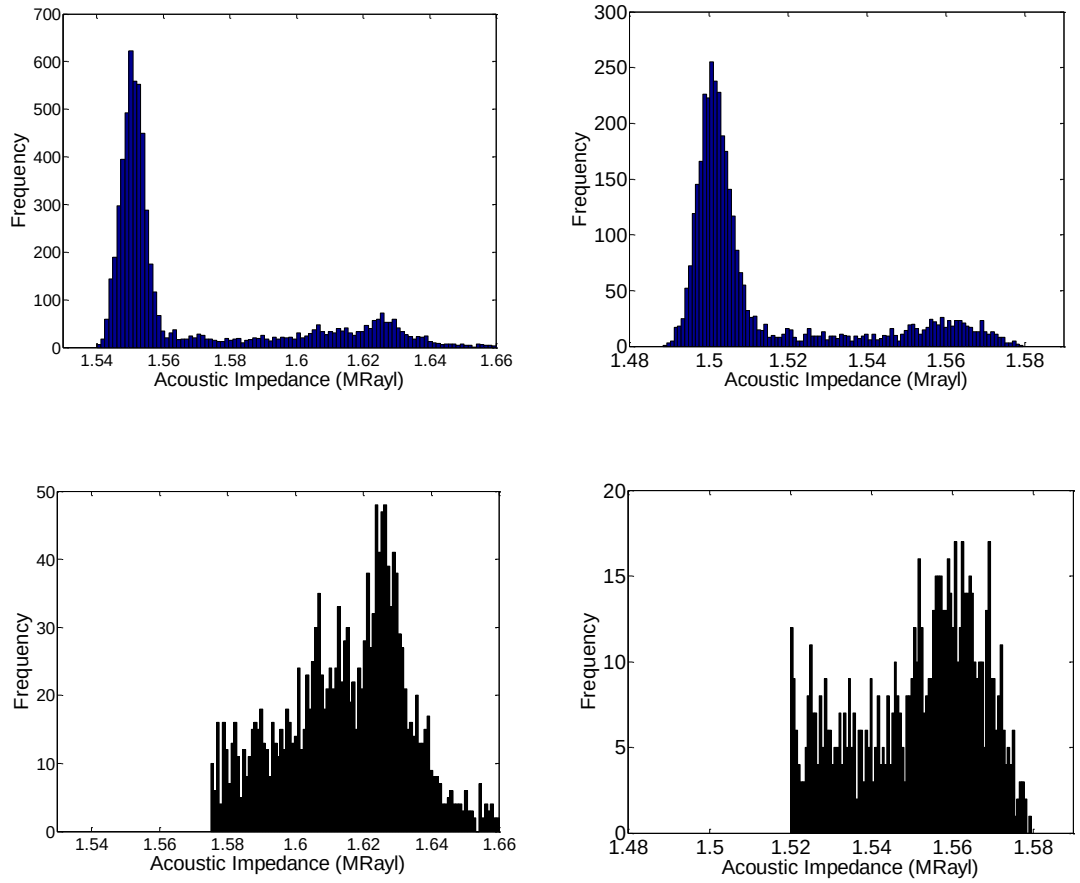

Figure 3.6 Histograms of the corrected acoustic impedance images of live and fixed clustered cells. Live cells histograms are presented on the left with media as the background. Fixed cells histograms are presented on the right with PBS as the background. The top histograms are for the corrected acoustic impedance images. The bottom histograms are for the corrected acoustic impedance images after applying a threshold to eliminate the background.

	Average Acoustic Impedance (MRayl)		Average Standard Deviation (MRayl)	
	3µm disk erosion	7µm disk erosion	3µm disk erosion	7µm disk erosion
Single-Live Cells	1.6029±0.0061	1.5978±0.0058	0.0142±0.0031	0.0120±0.0029
Clustered-Live Cells	1.6124±0.0081	1.6071±0.0090	0.0186±0.0026	0.0168±0.0027
Clustered-Fixed Cells	1.5524±0.0034	1.5481±0.0036	0.0172±0.0031	0.0152±0.0030

Table 3.2 Results of the average acoustic impedance and standard deviation for single-live cells, clustered-live cells and clustered-fixed cells using both 3µm and 7µm disk erosion.

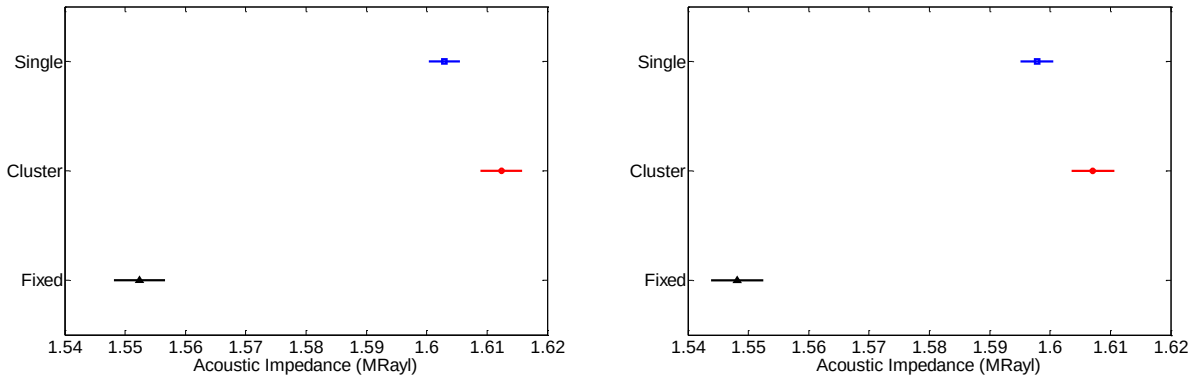

Figure 3.7 Comparison of the acoustic impedance values of the three different groups. Red circles, blue squares and black triangles represent average acoustic impedance of single-live cells, clustered-live cells and clustered-fixed cells respectively. Left and right plots are the results using 3µm and 7µm disks erosion respectively.

3.2 IMAGE ANALYSIS

3.2.1 SIZE COMPARISON

To compare the morphology of the acoustic impedance images with the fluorescence images, trace lines were used. Sizes of structures derived from the normalized trace line of acoustic impedance images, and fluorescence images labeled by Hoechst and CellTracker Orange for 20 single cells were calculated. The average size ratio of fluorescence images labeled by CellTracker Orange to acoustic impedance images was 1.02±0.08. The average size ratio of fluorescence images labeled by Hoechst over acoustic impedance images was 0.63±0.11.

3.2.2 ACQUIRING THE AVERAGE ACOUSTIC IMPEDANCE OF CELLS

Threshold and erosion operations were applied to segment the 37 corrected acoustic impedance images cells from the background. 20 of the images were images of single-live cells, 10 were of clustered-live cells, and 7 were of clustered-fixed cells. The histograms of a live and a fixed corrected acoustic impedance images before and after applying the threshold are

presented in figure 3.6. The image analysis processes of threshold and erosion for a single-live cell, clustered-live cells, and clustered-fixed cells are presented in figure 3.5. The average acoustic impedance and standard deviation of the segmented cells, after applying the threshold, and 3µm and 7µm in diameter erosion disks, are presented in table 3.3 for all three groups. The average acoustic impedance values of these three different groups were compared using multiple comparison tests. The results are shown in figure 3.7. In both cases, using 3µm and 7µm erosion disks, all three groups have average acoustic impedance values that are significantly different.

3.3 CONFOCAL IMAGES

The 3D morphology of MCF-7 cells was obtained using confocal microscopy. 16 fixed cells were imaged with both the Hoechst and CellTracker Orange stains. The average depth of the nucleus from the substrate was calculated by comparing the Hoechst and CellTracker Orange stains. Cross-sectional images of two cells are presented in figure 3.8. The average distance between the nucleus and the polystyrene substrate was measured to be 0.60±1.40µm.

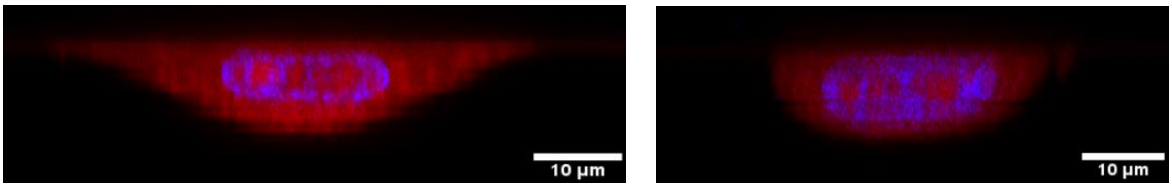

Figure 3.8 Cross-sectional image of fixed MCF-7 cells using confocal microscopy. The distance from the top of the cytoplasm (red, stained with Celltracker Orange), to the top of the nucleus (blue, stained with Hoechst) are 1µm and 0.66µm respectively.

3.4 SIMULATIONS

COMSOL simulations were performed to understand the capability of a 375MHz transducer to differentiate between two consecutive impedance mismatches at a distance less

than the wavelength. The results are presented in figure 3.9. In the case of an impedance mismatch of 0.3MRayl (solutions 1 and 2), two boundaries with a distance less than ~1.5µm will have an impact on the measured acoustic impedance. As the acoustic impedance mismatch decreases to 0.1MRayl (solutions 3 and 4), two boundaries with a distance less than ~0.7µm will have an impact on the measured acoustic impedance.

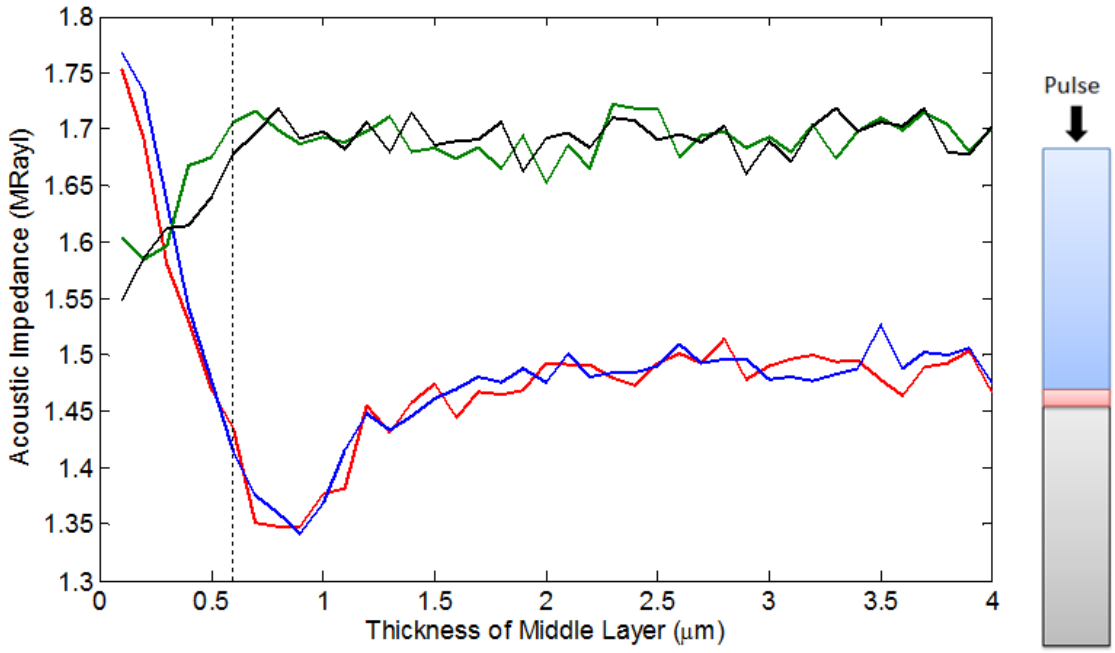

Figure 3.9 Simulation of the measured acoustic impedance vs. thickness of the middle layer (pink). Red, blue, green and black lines are results of the simulations 1, 2, 3 and 4 from table 2.1 ($\lambda = 4\mu m$). The dashed line represents the average distance between the nucleus and the substrate.

CHAPTER 4: DISCUSSION, CONCLUSION AND FUTURE WORK

4.1 DISCUSSION

Multiple features can be extracted by comparing the radiofrequency signal reflected from the cancerous cell and the media (figure 3.1). First, the amplitude of the reflected signal from the cancerous cell is less than the amplitude of the reflected signal from the media, as can be seen from figure 3.1 at approximate time interval of 1.390µs-1.405µs. This is due to the acoustic impedance mismatch between the polystyrene and the cancerous cell being less than the acoustic impedance mismatch between the polystyrene and the media. Second, by comparing the time interval of 1.405µs-1.415µs in figure 3.1, the amplitude of the reflected signal from the cell is higher than the amplitude of the reflected signal from the media. This time interval is correlated to the acoustic impedance mismatch within the media (black) and the cell (red). In case of the media, the amplitude of the reflected signal in this time interval is similar to noise (time interval 1.380µs-1.390µs). Therefore the acoustic impedance mismatch within the media itself is too small to generate a detectable signal. In contrast, the amplitude of the reflected signal at this time interval in case of a cancer cell is detectable (above the noise floor). This is because of the acoustic impedance mismatch within the heterogeneous single cancer cell. Third, the amplitude of the reflected signal at the time interval of 1.420µs-1.440µs in figure 3.1 is similar between the media and the cell. The signal at this time interval is due to the leaky Rayleigh waves reflected from the coupling fluid (water) and the polystyrene boundary. Leaky Rayleigh waves are the reemission of Rayleigh waves created at the polystyrene surface [66]. Since the setup at this boundary is exactly the same in case of media and cell, the reflected signal has the same amplitude. Finally, it is notable that the

radiofrequency signal indicates a change in the focal point in case of acoustic impedance imaging vs. acoustic microscopy imaging. In the case of acoustic microscopy imaging, the reflected signal peaks at around 1.460μs, while in case of acoustic impedance imaging the signal peaks at around 1.400μs. The change in the peak of the reflected signal is due to the higher speed of sound in the polystyrene compared to the coupling fluid and the refocusing which occurs as the ultrasound waves enter the polystyrene layer (this is due to the acoustic impedance mismatch between coupling fluid and polystyrene).

The setup of this experiment requires the ultrasound waves to propagate through the polystyrene layer before they reach the sample. A calibration was applied to account for the finite angle of the transducer as the ultrasound waves enter the polystyrene layer as well as for the shear waves created in the polystyrene layer. The relation before applying the calibration (apparent acoustic impedance) and after applying the calibration (true acoustic impedance) is demonstrated in figure 3.2. The apparent acoustic impedance and the true acoustic impedance are equal at the acoustic impedance of the reference (Z_r). In the case of media (red), PBS (blue), or air (black) as a reference, the apparent and true acoustic impedance coincide at 1.55MRayl, 1.50MRayl, or 0.0004MRayl, respectively. In addition, extrapolating the three curves in figure 3.2 intersect at the apparent acoustic impedance of 2.46MRayl. This intersection occurs at the acoustic impedance of the polystyrene, which can be interpreted as absence in the reflected signal. At this acoustic impedance the reference does not play a factor in the measured acoustic impedance.

The results of the AIIM experiment suggest that the nucleus is unlikely to be a strong scattering source in cancer cells. Acoustic impedance images were unable to detect the presence of the nucleus (figure 3.3), suggesting that the nucleus has an acoustic impedance similar to the surrounding cytoplasm. Moreover, the average size ratio of the cytoplasm over the acoustic impedance images was approximately 1 (1.02±0.08). On the other hand, the average size ratio of the nucleus over the acoustic impedance images was < 1 (0.63±0.11). This contradicts the hypothesis of the nucleus being the major scattering source [33-35]. However, using AIIM to attain 2D images and identifying exactly which cellular component is being imaged is challenging, as the distances between the microstructures and substrate are not known. Identifying the exact scattering source is challenging because AIIM is a 2D technique focused on slide-sample interface, while the ultrasound waves may not be able to access the cellular component at various depths. Also, it is not known how close to the substrate a structure has to be for the AIIM to measure an acoustic impedance value related to the microstructure rather than the cytoplasm.

To measure the distance between the nucleus and the polystyrene substrate, confocal microscopy was used. Figure 3.4 shows that fixing a cell preserves its gross architecture, which is in agreement with previous research [67, 68]. Confocal images revealed the distance of the nucleus to the substrate is 0.60±1.40µm. COMSOL simulations were performed to better understand the effect of this distance on the measured acoustic impedance values. The results in figure 3.9 suggest that if the acoustic impedance mismatch between the nucleus and the cytoplasm is 0.3MRayl or 0.1MRayl, then the nucleus at depths from the substrate ranges between 0.1-1.5µm or 0.1-0.7µm, respectively, would have an impact on AIIM. It can be

inferred, as the acoustic impedance mismatch between the nucleus and the cytoplasm decreases, it is less likely to detect the nucleus in acoustic impedance images. Since the nucleus was not detected in the acoustic impedance images, the acoustic impedance mismatch between the nucleus and the cytoplasm has to be less than 0.1MRayl (figure 3.9). An exact value of the acoustic impedance of the nucleus was not obtained.

The COMSOL simulations setup resembles the effect of thin-film interference, except that the incident wave is pulsed and not continuous. Thin-film interference occurs when two consecutive boundaries with acoustic impedance mismatches are separated by a distance approximately equal to the wavelength of the ultrasound wave, or integer multiples of the wavelength (for small integer values, depending on the attenuation of the wave within the film). In this case the wave reflected at the first boundary interferes with the wave reflected at the second boundary. This interference can be constructive, destructive or in-between, depending on the distance between the two consecutive boundaries. The first constructive or destructive interference occurs at 1/4 of the wavelength, because the wave reflected from the second boundary travels the distance twice compared to the wave reflected from the first boundary, which creates a phase shift of $\pi/2$. Constructive interference occurs in case of one phase shift upon reflection at the first or second boundary. Destructive interference occurs in case of no phase shift or two phase shifts at the first and second boundaries. Phase shift occurs when the wave travels from a material of lower acoustic impedance to a material of higher acoustic impedance, which results into a shift of $\pi/2$. In simulations 1 and 2 (red and blue lines in figure 3.9) the first constructive interference is noted at thickness of approximately 1µm which is approximately 1/4 the wavelength of ultrasound wave in the coupling fluid. Also, it is a

constructive interference as there is one phase shift at the cytoplasm to nucleus boundary. In simulations 3 and 4 (green and black lines in figure 3.9) the interference between the two reflected waves was also noted, but it faded quicker because the acoustic impedance mismatch in the second boundary is three times lower than in the simulations 1 and 2. In addition, the relation between the calculated acoustic impedance values from the simulations and the thickness of the middle layer in simulations 3 and 4 initially increases, in contrast to simulations 1 and 2 which initially decreases. This is because there is no phase shift upon reflection in the radiofrequency signals of simulations 3 and 4. Finally, it can be observed from figure 3.9 that the results are not directly related to the speed of sound and the density parameters. Instead it is directly related to the final product of the speed of sound and the density (acoustic impedance). This is inferred from the similarity in the results of simulations 1 & 2, and 3 & 4.

Using AIIM, we were able to measure the average acoustic impedance of cancerous cells. AIIM accuracy was verified by measuring the average acoustic impedance of water, which compared to the literature, had a percent error of 0.19%. The average acoustic impedance for single-live cancer cells was calculated to be 1.60±0.01MRayl, which is higher than 1.56±0.01MRayl for MCF-7, previously obtained using time-resolved acoustic microscopy [55]. Other cancer cells have been reported to have varying acoustic impedances [38, 54, 56]. The measured standard deviation of single-live cells (0.0142MRayl) is approximately 16 times higher than water (0.0009MRayl). This increase is due to the impedance variation within a single cell as shown in figure 3.3 and figure 3.1 at the time interval of 1.405 μs-1.415 μs. In addition, the average acoustic impedance and standard deviation results for clustered-live cells and clustered-fixed cells are presented in table 3.2.

Two observations have been noted in this study. First, a significant increase in the average acoustic impedance of clustered vs. single live cells as shown in figure 3.7. A reasonable explanation is clustered cells support more cell to cell communications (e.g. gap junctions), which allows various molecules and ions to pass in-between cells [69]. The molecules and ions act as a signal for gene and protein expression which can lead to changes in the cell physiology. The second observation is the significant decrease in the average acoustic impedance of fixed clustered cells vs. live clustered cells using a 3μm and 7μm erosion disk as shown in figure 3.7. Previous experiments report an increase in density and decrease in speed of sound in fixed cells [70-72]. In conclusion, AIIM was able to differentiate between single-live cells, clustered-live cells and clustered-fixed cells by comparing the average acoustic impedance values.

The image analysis operations used in the experiments can have an impact on the measured average acoustic impedance values. The effect of using different erosion disks on the average acoustic impedance values is demonstrated in figure 3.7 and table 3.2 by using two different erosion disks of 3μm and 7μm. The results showed using larger erosion disk (7μm) led to a decrease in the average acoustic impedance values of all single-live cell, clustered-live cells, and clustered-fixed cells. This suggests that the edges have a higher average acoustic impedance values than the rest of the cell(s) (figure 3.3). The increase in the average acoustic impedance values at the edges could be due to significant physiological changes inside the cell or an effect created from the interaction of ultrasound waves with the edges. Moreover, the threshold operation can also play a factor on the final measured average acoustic impedance values. Although the effect of different threshold values on the average acoustic impedance was not tested in this thesis, different methods to acquire the threshold values will have an

impact on it. Two different backgrounds were used in the experiment. The different backgrounds used in these experiments should not affect the measured average acoustic impedance values due to the fact that a correction was applied to account for each specific background (PBS and media).

This study provides support for the finding that the whole cell acts as one scattering source as opposed to the nucleus being the dominant scatterer source [33-35]. There are several possible reasons for this discrepancy. First, the assumptions used in this experiment are different than the assumptions used in calculating BSC, which has been used to predict the scatterer source. These assumptions required for the analysis of the experimental data are: the boundary between the polystyrene substrate and the sample is semi-infinite and MCF-7 cells have inviscous properties. Secondly, the frequency, cell line and background used in these experiments are different than in the previous studies. The frequency used can have an impact on the results as changing frequencies can affect its sensitivity to differently sized scatterers. Cell line is also a factor as other cancer cells have been reported to have varying acoustic impedances [38, 54, 56]. Finally, the background that a scattering source is positioned within will have an impact on determining the dominant scattering source. This was done by comparing the backscattered signal of cells in suspension and in pellets [73]. The spectral data suggested that the nucleus is the dominant scatterer source in case of pellets while the whole cell is the dominant scatterer source in case of suspension.

This study was unable to measure the acoustic impedance of identifiable microstructures in cancer cells (e.g. nucleus). This is likely due to the distance between the

nucleus and the substrate. This distance made it impossible to acquire a reflected signal due to the acoustic impedance mismatch between the substrate and the nucleus. A way to improve this study is to segment each acoustic impedance images into two different compartments. One compartment correlates to the position of the nucleus and the other to the position of the cytoplasm, both acquired from the fluorescence image.

In this work, the AIIM was used to measure the 2D acoustic impedance map of MCF-7 cells attached to the polystyrene substrate. The use of AIIM for measuring the acoustic impedance of biological microstructures has been previously described in a conference paper by Hozumi et. al. [57]. Other methods have been used to measure the acoustic impedance of biological structures [38, 55, 58, 74]. The two main advantages of AIIM are: it does not apply physical stress to the biological structures and it can be used to acquire 2D acoustic impedance maps. Two applications can be acquired from the spatial acoustic impedance maps. First, the average acoustic impedance values can be used to acquire information about the physiological state of cancer cells. Second, the acoustic impedance fluctuations can be used to predict the backscattered signal in tissues composed of cancer cells. Such measurements are used in the 3DZM method (by comparing the backscattered signal to the theoretical backscattered signal) to identify the major scattering source in biological structures (anatomical structures). Understanding the acoustic impedance variations within cells has the potential to improved ultrasound techniques that can be used to detect anatomical and physiological changes. This can lead to increase in the use of ultrasound to diagnose certain medical conditions, as well as to monitor patient response to treatments.

4.2 CONCLUSION

This work measures, for the first time, the acoustic impedance images of cancer cells using AIIM. The morphology of acoustic impedance images can be used to better understand the mechanical properties of cell microstructures and relate it to the scatterer source in cancer tissues. This can lead to more accurate QUS parameters and a better correlation of these parameters to tissue microstructures. The acoustic impedance images in this study were compared to fluorescent and confocal images with the cell nucleus and cytoplasm stained. The results show that acoustic impedance images were unable to detect the presence of the nucleus.

In addition to detecting anatomical changes through evaluating the scattering source, acoustic impedance images can be used to evaluate physiological changes through measuring average acoustic impedance values. In this study three different groups of cells (single-live cells, clustered-live cells, and clustered-fixed cells) were differentiated by measuring the average acoustic impedance values.

4.3 FUTURE WORK

AIIM can be used to acquire an accurate 3DZM of soft tissues. This can be done by slicing the tissues into thin slices and then taking an image of them using AIIM. Then the acoustic impedance images are combined to obtain a 3DZM. The 3DZM acquired using AIIM can calculate acoustic impedance variation within the sample and accounts for wider ranges of change that the preceding 3DZM lacked. This can improve 3DZM by using it to acquire form factors and scatterer sources of specific tissues.

Dissimilar tissues can have various scattering sources and can scatter an ultrasound wave differently at different frequencies. Therefore, more cell types and tissues with extracellular structures need to be imaged at different frequencies using AIIM. For a cell types to be imaged using AIIM, it has to adhere to the substrate and has to have a size larger than the lateral resolution of the transducer. Regarding the frequency used in AIIM, the higher the frequency the better spatial resolution of the measurement and the more accurate the semi-infinite boundary assumption is (equation 2.4). However, higher frequencies have higher attenuation and therefore thinner substrate is required for the measurement to have an adequate signal-to-noise.

AIIM has been used to measure the acoustic impedance of cancer cells at the substrate-sample interface. However, the method cannot detect the acoustic impedance of microstructures away from the substrate. Increasing the pulse length, can create a phenomenon similar to the thin film interference in optics, thereby potentially increasing the sensitivity of the measurement of such structures. This can make it possible to measure the acoustic impedance of the nucleus.

Confocal and acoustic microscopy systems built together will make it possible to obtain both acoustic and confocal images of the same cell. The system can be used to acquire the distance between the nucleus and the substrate of a specific cell without fixing it. This can be used to acquire the acoustic impedance of the nucleus. In addition, the fluorescent images can be replaced with higher contrast confocal images. In the experiments presented in this work,

the presence of the background between the sample and the fluorescence microscopy caused the images to have low contrast.

CHAPTER 5: APPENDIX

5.1 SUPPLEMENTAL DATA USING 3μM EROSION DISK

Cell Number	**Average acoustic Impedance (MRayl)**	**Standard deviation of acoustic impedance (MRayl)**	**Number of pixels**	**Trace line size of Cytoplasm / acoustic image**	**Trace line size of Nucleus / acoustic image**
Single Live Cells					
1	1.6022	0.0150	687	20/21	14/21
2	1.5973	0.0091	628	28/26	14/26
3	1.6024	0.0129	363	27/29	17/29
4	1.5959	0.0124	295	21/22	13/22
5	1.5968	0.0126	481	20/18	14/18
6	1.5975	0.0130	491	17/19	14/19
7	1.6040	0.0123	789	20/21	11/21
8	1.5909	0.0069	630	38/35	16/35
9	1.5989	0.0149	167	24/23	14/23
10	1.6122	0.0197	713	21/24	13/24
11	1.6077	0.0187	569	23/22	17/22
12	1.6034	0.0140	536	32/35	19/35
13	1.6112	0.0145	659	26/24	17/24
14	1.6070	0.0150	541	34/30	13/30
15	1.6021	0.0155	573	26/24	17/24
16	1.6018	0.0155	449	18/18	10/18
17	1.6021	0.0147	467	17/18	13/18
18	1.6105	0.0137	636	23/21	16/21
19	1.6001	0.0137	1250	30/29	17/29
20	1.6145	0.0201	449	22/20	15/20
Average	1.6029±0.0061	0.0142±0.0031	569±218	1.02±0.08	0.63±0.11
Clustered Live Cells					
1	1.6129	0.0183	723		
2	1.6147	0.0184	1406		
3	1.6236	0.0222	1089		

4	1.6168	0.0189	1596
5	1.6126	0.0182	702
6	1.6109	0.0230	630
7	1.6212	0.0184	1894
8	1.5954	0.0135	387
9	1.6044	0.0172	109
10	1.6111	0.0175	1359
Average	1.6124±0.0081	0.0186±0.0026	990±570
Fixed Clustered Cells			
1	1.5519	0.0165	464
2	1.5526	0.0193	1416
3	1.5493	0.0184	279
4	1.5592	0.0196	1086
5	1.5535	0.0203	1323
6	1.5506	0.0126	606
7	1.5494	0.0135	473
Average	1.5524±0.0034	0.0172±0.0031	807±459

5.2 Supplemental Data Using 7μM Erosion Disk

Cell Number	**Average acoustic Impedance (MRayl)**	**Standard deviation of acoustic impedance (MRayl)**	**Sample Number**
Single Live Cells			
1	1.5991	0.0145	375
2	1.5927	0.0078	475
3	1.5986	0.0116	235
4	1.5917	0.0102	149
5	1.5944	0.0110	259
6	1.5945	0.0110	223
7	1.5991	0.0105	551
8	1.5879	0.0065	415
9	1.5926	0.0101	70
10	1.6056	0.0175	457
11	1.6001	0.0160	324
12	1.6000	0.0116	368

13	1.6101	0.0137	474
14	1.6010	0.0123	378
15	1.5932	0.0105	225
16	1.5968	0.0130	172
17	1.5942	0.0115	249
18	1.6017	0.0107	248
19	1.5939	0.0111	848
20	1.6091	0.0184	323
Average	1.5978±0.0058	0.0120±0.0029	341±172
Cluster Live Cells			
1	1.6061	0.0162	506
2	1.6107	0.0167	1032
3	1.6184	0.0207	788
4	1.6126	0.0177	1265
5	1.6082	0.0167	524
6	1.6036	0.0201	436
7	1.6176	0.0171	1642
8	1.5889	0.0110	1642
9	1.5968	0.0158	814
10	1.6080	0.0156	999
Average	1.6071±0.0090	0.0168±0.0027	965±441
Fixed Clustered Cells			
1	1.5482	0.0149	554
2	1.5480	0.0172	1030
3	1.5439	0.0156	168
4	1.5546	0.0180	825
5	1.5501	0.0182	986
6	1.5480	0.0111	443
7	1.5442	0.0113	294
Average	1.5481±0.0036	0.0152±0.0030	614±339

REFERENCES

[1] G. Kossoff, "Display techniques in ultrasound pulse echo investigations: A review," *J. Clin. Ultrasound,* vol. 2, pp. 61-72, 1974.

[2] T. L. Szabo, *Diagnostic Ultrasound Imaging: Inside Out.* Burlington, MA: Elsevier Academic Press, 2004.

[3] M. L. Oelze, J. O'Brien William D., J. P. Blue and J. F. Zachary, "Differentiation and characterization of rat mammary fibroadenomas and 4T1 mouse carcinomas using quantitative ultrasound imaging," *IEEE Transactions on Medical Imaging*, pp. 764-771, 2004.

[4] M. L. Oelze and J. F. Zachary, "Examination of cancer in mouse models using high-frequency quantitative ultrasound," *Ultrasound Med. Biol.,* vol. 32, pp. 1639-1648, 2006.

[5] D. P. Hruska, J. Sanchez and M. L. Oelze, "Improved diagnostics through quantitative ultrasound imaging," *Proceedings of the 31st Annual International Conference of the IEEE EMBS*, pp. 1956-1959, 2009.

[6] J. Kemmerer, G. Ghoshal and M. Oelze, "Quantitative ultrasound assessment of HIFU induced lesions in rodent liver," *J. Acoust. Soc. Am.,* pp. 1396-1399, 2010.

[7] A. P. Sarvazyan, "Ultrasonic velocimetry of biological compounds," *Annual Review of Biophysics and Biophysical Chemistry,* vol. 20, pp. 321-342, 1991.

[8] Lee JK, Dixon WT, Ling D, Levitt RG, Murphy WA Jr., "Fatty infiltration of the liver: demonstration by proton spectroscopic imaging. Preliminary observations," *Radiology,* vol. 1, pp. 195-201, 1984.

[9] Anonymous "Cirrhosis: Diagnosis with Sonographic Study of the Liver Surface," *Journal of Diagnostic Medical Sonography,* vol. 5, pp. 345-345, 1989.

[10] K. Shung and G. Thieme, Eds., *Ultrasonic Scattering in Biological Tissues.* Boca Raton, FLorida: CRS Press, 1993.

[11] G. Mathis, *Chest Sonography.* Berlin: Springer-Verlag, 2011.

[12] S. Carkaci, L. Santiago, B. E. Adrada and G. J. Whitman, "Screening for breast cancer with sonography," *Semin. Roentgenol.,* vol. 46, pp. 285, 2011.

[13] J. Mamou, M. L. Oelze, J. O'Brien William D. and J. F. Zachary, "Identifying ultrasonic scattering sites from three-dimensional impedance maps," *J. Acoust. Soc. Am.,* vol. 117, pp. 413, 2005.

[14] E. Tohno, E. Ueno and H. Watanabe, "Ultrasound screening of breast cancer," *Breast Cancer,* vol. 16, pp. 18-22, 2009.

[15] S. Suresh, J. Spatz, J. P. Mills, A. Micoulet, M. Dao, C. T. Lim, M. Beil and T. Seufferlein, "Connections between single-cell biomechanics and human disease states: gastrointestinal cancer and malaria," *Acta Biomaterialia,* vol. 1, pp. 15-30, 2005.

[16] R. S. C. Cobbold, *Foundations of Biomedical Ultrasound.* Oxford: Oxford University Press, 2007.

[17] O. Falou, "Modelling High Frequency Ultrasound Scattering From Cells and Ultrasound Contrast Agents," *Digital Commons @ Ryerson,* 2011.

[18] J. James J. Faran, "Sound Scattering by Solid Cylinders and Spheres," *J. Acoust. Soc. Am.,* vol. 23, pp. 405, 1951.

[19] K. Shung and G. Thieme, Eds., *Ultrasonic Scattering in Biological Tissues.* Boca Raton Ann Arbor London Tokyo: 1993.

[20] L. X. Yao, J. A. Zagzebski and E. L. Madsen, "Backscatter coefficient measurements using a reference phantom to extract depth-dependent instrumentation factors," *Ultrason. Imaging,* vol. 12, pp. 58-70, 1990.

[21] J. J. Anderson, J. O'Brien William D., T. J. Hall, M. Herd, M. R. King, A. Haak, Z. T. Hafez, J. Song, M. L. Oelze, E. L. Madsen and J. A. Zagzebski, "Interlaboratory comparison of backscatter coefficient estimates for tissue-mimicking phantoms," *Ultrason. Imaging,* vol. 32, pp. 48, 2010.

[22] M. F. Insana, R. F. Wagner, D. G. Brown and T. J. Hall, "Describing small-scale structure in random media using pulse-echo ultrasound," *J. Acoust. Soc. Am.,* vol. 87, pp. 179, 1990.

[23] J. Mamou, E. J. Feleppa, A. Coron, M. L. Oelze, E. Saegusa-Beecroft, M. Hata, P. Lee, J. Machi, E. Yanagihara and P. Laugier, "Three-dimensional high-frequency backscatter and envelope quantification of cancerous human lymph nodes," *Ultrasound Med. Biol.,* vol. 37, pp. 345-357, 2011.

[24] M. F. Insana, J. G. Wood and T. J. Hall, "Identifying acoustic scattering sources in normal renal parenchyma in vivo by varying arterial and ureteral pressures," *Ultrasound Med. Biol.,* vol. 18, pp. 587, 1992.

[25] K. A. Wear, "Ultrasonic Characterization of the Heart (Myocardium)," 1987.

[26] Frederic L. Lizzi, Michael Greenebaum, Ernest J. Feleppa, Marek Elbaum and D. Jackson Coleman, "Theoretical framework for spectrum analysis in ultrasonic tissue characterization," *J. Acoust. Soc. Am.,* vol. 73, pp. 1366, 1983.

[27] F. L. Lizzi, M. Ostromogilsky, E. J. Feleppa, M. C. Rorke and M. M. Yaremko, "Relationship of ultrasonic spectral parameters to features of tissue microstructure," *IEEE Trans. Ultrason. Ferroelectr. Freq. Control,* vol. 34, pp. 319-329, 1987.

[28] E. J. Feleppa, F. L. Lizzi, D. J. Coleman and M. M. Yaremko, "Diagnostic spectrum analysis in ophthalmology: a physical perspective," *Ultrasound Med. Biol.,* vol. 12, pp. 623-631, 1986.

[29] L. A. Clifford, "On the first-order amplitude statistics of myocardial ultrasonic backscatter," 1996.

[30] J. C. Bamber and C. R. Hill, "Acoustic properties of normal and cancerous human liver-I. Dependence on pathological condition," *Ultrasound Med. Biol.,* vol. 7, pp. 121-133, 1981.

[31] D. H. Turnbull, S. R. Wilson, A. L. Hine and F. S. Foster, "Ultrasonic characterization of selected renal tissues," *Ultrasound Med. Biol.,* vol. 15, pp. 241-253, 1989.

[32] M. C. Kolios, G. J. Czarnota, M. Lee, J. W. Hunt and M. D. Sherar, "Ultrasonic spectral parameter characterization of apoptosis," *Ultrasound Med. Biol.,* vol. 28, pp. 589-597, 2002.

[33] M. C. Kolios, L. Taggart, R. Baddour, F. Foster, J. Hunt, G. Czarnota and M. Sherar, "An Investigation of Backscatter Power Spectra from Cells, Cell Pellets and Microspheres," *IEEE International Ultrasonics Symposium,* 2003.

[34] L. R. Taggart, R. E. Baddour, A. Giles, G. J. Czarnota and M. C. Kolios, "Ultrasonic Characterization of Whole Cells and Isolated Nuclei," *Ultrasound Med. Biol.,* vol. 33, pp. 389-401, 2007.

[35] G. J. Czarnota, M. C. Kolios, J. Abraham, M. Portnoy, F. P. Ottensmeyer, J. W. Hunt and M. D. Sherar, "Ultrasound imaging of apoptosis: high-resolution non-invasive monitoring of programmed cell death in vitro, in situ and in vivo," *Br. J. Cancer,* vol. 81, pp. 520-527, 1999.

[36] J. Mamou, M. L. Oelze, J. O'Brien William D. and J. F. Zachary, "Extended three-dimensional impedance map methods for identifying ultrasonic scattering sites," *J. Acoust. Soc. Am.,* vol. 123, pp. 1195, 2008.

[37] E. C. Naylor, R. E. B. Watson and M. J. Sherratt, "Molecular aspects of skin ageing," *Maturitas,* vol. 69, pp. 249-256, 2011.

[38] E. C. Weiss, P. Anastasiadis, G. Pilarczyk, R. M. Lemor and P. V. Zinin, "Mechanical properties of single cells by high-frequency time-resolved acoustic microscopy," *IEEE Trans. Ultrason. Ferroelectr. Freq. Control,* vol. 54, pp. 2257, 2007.

[39] E. Fuchs and K. Weber, "Intermediate Filaments: Structure, Dynamics, Function and Disease," *Annu. Rev. Biochem.,* vol. 63, pp. 345-382, 1994.

[40] G. Bao and S. Suresh, "Cell and molecular mechanics of biological materials," *Nature Materials,* vol. 2, pp. 715-725, 2003.

[41] D. E. Ingber, "Mechanical Signaling and the Cellular Response to Extracellular Matrix in Angiogenesis and Cardiovascular Physiology," *Circulation Research: Journal of the American Heart Association,* vol. 91, pp. 877-887, 2002.

[42] R. Suwanarusk, B. M. Cooke, A. M. Dondorp, K. Silamut, J. Sattabongkot, N. J. White and R. Udomsangpetch, "The Deformability of Red Blood Cells Parasitized by," *J. Infect. Dis.,* vol. 189, pp. 190-194, 2004.

[43] X. Zhao, R. Akhtar, N. Nijenhuis, S. J. Wilkinson, L. Murphy, C. Ballestrem, M. J. Sherratt, R. E. B. Watson and B. Derby, "Multi-layer phase analysis: quantifying the elastic properties of soft tissues and live cells with ultra-high-frequency scanning acoustic microscopy," *IEEE Trans. Ultrason. Ferroelectr. Freq. Control,* vol. 59, pp. 610-620, 2012.

[44] P. Boutouyrie, A. I. Tropeano, R. Asmar, I. Gautier, A. Benetos, P. Lacolley and S. Laurent, "Aortic stiffness is an independent predictor of primary coronary events in hypertensive patients: a longitudinal study," *Hypertension,* vol. 39, pp. 10-15, 2002.

[45] S. Aoun, J. Blacher, M. E. Safar and J. J. Mourad, "Diabetes mellitus and renal failure: effects on large artery stiffness," *J. Hum. Hypertens.,* vol. 15, pp. 693, 2001.

[46] K. Cruickshank, L. Riste, S. G. Anderson, J. S. Wright, G. Dunn and R. G. Gosling, "Aortic pulse-wave velocity and its relationship to mortality in diabetes and glucose intolerance: an integrated index of vascular function?" *Circulation,* vol. 106, pp. 2085-2090, 2002.

[47] P. Grybauskas, K. Kundrotas, V. Sukackas and E. Yaronis, "Ultrasonic digital interferometer for investigation of blood clotting," *Ultrasonics,* vol. 16, pp. 33-36, 1978.

[48] M. Radmacher, M. Fritz and P. K. Hansma, "Imaging soft samples with the atomic force microscope: gelatin in water and propanol," *Biophysical Journal,* vol. 69, pp. 264-270, 1995.

[49] Marina Puig-De-Morales, Mireia Grabulosa, Jordi Alcaraz, Joaquim Mullol, Geoffrey N. Maksym, Jeffrey J. Fredberg and Daniel Navajas, "Measurement of cell microrheology by magnetic twisting cytometry with frequency domain demodulation," *J. Appl. Physiol.,* vol. 91, pp. 1152-1159, 2001.

[50] A. Ashkin and J. M. Dziedzic, "Optical Trapping and Manipulation of Viruses and Bacteria," *Science,* vol. 235, pp. 1517-1520, 1987.

[51] D. Chapman, "Mechanics and thermodynamics of biomembranes," *FEBS Lett.,* vol. 142, pp. 179-180, 1982.

[52] S. Usami, H. H. Chen, Y. Zhao, S. Chien and R. Skalak, "Design and construction of a linear shear stress flow chamber," *Ann. Biomed. Eng.,* vol. 21, pp. 77-83, 1993.

[53] J. H. Wang, P. Goldschmidt-Clermont and F. C. Yin, "Contractility affects stress fiber remodeling and reorientation of endothelial cells subjected to cyclic mechanical stretching," *Ann. Biomed. Eng.,* vol. 28, pp. 1165-1171, 2000.

[54] T. Kundu, J. Bereiter-Hahn and I. Karl, "Cell property determination from the acoustic microscope generated voltage versus frequency curves," *Biophys. J.,* vol. 78, pp. 2270-2279, 2000.

[55] E. Strohm, G. J. Czarnota and M. C. Kolios, "Quantitative measurements of apoptotic cell properties using acoustic microscopy," *IEEE Trans. Ultrason. Ferroelectr. Freq. Control,* vol. 57, pp. 2293-2304, 2010.

[56] T. Kundu, J. Bereiter-Hahn and K. Hillmann, "Measuring elastic properties of cells by evaluation of scanning acoustic microscopy V(Z) values using simplex algorithm," *Biophys. J.,* vol. 59, pp. 1194-1207, 1991.

[57] N. Hozumi, A. Kimura, S. Terauchi, M. Nagao, S. Yoshida, K. Kobayashi and Y. Saijo, "Acoustic impedance micro-imaging for biological tissue using a focused acoustic pulse with a frequency range up to 100 MHz," *IEEE Ultrasonic Symposium,* vol. 1, pp. 170-173, 2005.

[58] Hozumi N., Hozumi N., Nakano A., Nakano A., Terauchi S.,Nagao M., Yoshida S., Kobayashi K., Yamamoto S., Saijo Y., "9D-1 precise calibration for biological acoustic impedance microscope," *IEEE Ultrasonic Symposium*, pp. 801-804, 2007.

[59] N. Hozumi, A. Kimura, S. Terauchi, M. Nagao, S. Yoshida, K. Kobayashi and Y. Saijo, "Acoustic impedance micro-imaging for biological tissue using a focused acoustic pulse with a frequency range up to 100 MHz," *IEEE Ultrasonic Symposium,* vol. 1, pp. 170-173, 2005.

[60] W. G. Mayer, "Energy partition of ultrasonic waves at flat boundaries," *Ultrasonics,* vol. 3, pp. 62-68, 1965.

[61] Jeff W Lichtman, José-Angel Conchello, "Fluorescence microscopy," *Nature Methods,* vol. 2, pp. 910-919, 2005.

[62] T. A. Beerman, M. M. McHugh, R. Sigmund, J. W. Lown, K. E. Rao and Y. Bathini, "Effects of analogs of the DNA minor groove binder Hoechst 33258 on topoisomerase II and I mediated activities," *BBA - Gene Structure and Expression,* vol. 1131, pp. 53-61, 1992.

[63] P. Dean, "Confocal microscopy: principles and practices," *Curr Protocols Cytometry,* pp. 2:8.1–2.8.12, 1998.

[64] Claxton Nathan, Fellers Thomas, Davidson Michael, "Laser Scanning Confocal Microscopy," *Encyclopedia of Medical Devices and Instrumentation,* 2006.

[65] F. S. Foster, C. J. Pavlin, K. A. Harasiewicz, D. A. Christopher and D. H. Turnbull, "Advances in ultrasound biomicroscopy," *Ultrasound Med. Biol.,* vol. 26, pp. 1-27, 2000.

[66] R. G. Maev, *Acoustic Microscopy: Fundamentals and Applications.* Weinheim: Wiley-VCH, pp. 15-16, 2008.

[67] J. W. Gillespie, R. L. Strausberg, J. I. Epstein, S. R. Hamilton, G. Gannot, G. V. Baibakova, V. S. Calvert, M. J. Flaig, R. F. Chuaqui, J. C. Herring, J. Pfeifer, C. J. M. Best, E. F. Petricoin, W. M. Linehan, P. H. Duray, G. S. Bova, M. R. Emmert-Buck, V. E. Bichsel, K. A. Cole, S. F. Greenhut, S. M. Hewitt, M. Ahram, Y. B. Gathright and M. J. Merino, "Evaluation of non-formalin tissue fixation for molecular profiling studies," *The American Journal of Pathology,* vol. 160, pp. 449-457, 2002.

[68] I. E. Chesnick, J. T. Mason, T. J. O'Leary and C. B. Fowler, "Elevated Pressure Improves the Rate of Formalin Penetration while Preserving Tissue Morphology," *Journal of Cancer,* vol. 1, pp. 178-183, 2010.

[69] J. Simek, J. Churko, Q. Shao and D. W. Laird, "Cx43 has distinct mobility within plasma-membrane domains, indicative of progressive formation of gap-junction plaques," *J. Cell. Sci.,* vol. 122, pp. 554-562, 2009.

[70] A. A. Brayman and M. W. Miller, "Cell density dependence of the ultrasonic degassing of fixed erythrocyte suspensions," *Ultrasound Med. Biol.,* vol. 19, pp. 243-252, 1993.

[71] A. K. Bryan, A. Goranov, A. Amon, S. R. Manalis and M. W. Kirschner, "Measurement of Mass, Density, and Volume during the Cell Cycle of Yeast," *Proc. Natl. Acad. Sci.,* vol. 107, pp. 999-1004, 2010.

[72] S. L. Baldwin, M. Yang, K. R. Marutyan, K. D. Wallace, M. R. Holland and J. G. Miller, "Measurements of the anisotropy of ultrasonic velocity in freshly excised and formalin-fixed myocardial tissue," *J. Acoust. Soc. Am.,* vol. 118, pp. 505, 2005.

[73] M. C. Kolios, G. J. Czarnota, A. Worthington, A. Giles, A. S. Tunis and M. D. Sherar, "Towards understanding the nature of high frequency backscatter from cells and tissues: An investigation

of backscatter power spectra from different concentrations of cells of different sizes," *IEEE Ultrasonic Symposium*, pp. 606-609, 2004.

[74] Xuegen Zhao, R. Akhtar, N. Nijenhuis, S. J. Wilkinson, L. Murphy, C. Ballestrem, M. J. Sherratt, R. E. B. Watson and B. Derby, "Multi-layer phase analysis: quantifying the elastic properties of soft tissues and live cells with ultra-high-frequency scanning acoustic microscopy," *IEEE Transactions on Ultrasonics, Ferroelectrics and Frequency Control,* vol. 59, pp. 610-620, 2012.